

MODEL ATMOSPHERES FOR G, F, A, B, AND O STARS

ROBERT L. KURUCZ*

Harvard-Smithsonian Center for Astrophysics

Received 1978 July 24; accepted 1978 October 11

ABSTRACT

A grid of LTE model atmospheres is presented for effective temperatures ranging from 5500 to 50,000 K, for gravities from the main sequence down to the radiation pressure limit, for abundances solar, 1/10 solar, and 1/100 solar. The models were computed by use of a statistical distribution-function representation of the opacity of almost 10^6 atomic lines. For each model we tabulate the temperature structure, fluxes, UBV and $uvby$ colors, bolometric correction, and Balmer line profiles. The solar abundance models are compared to narrow, intermediate (by Relyea and Kurucz), and wide (by Relyea and Kurucz and by Buser and Kurucz) band photometry and are found to be in good agreement with the observations for effective temperatures above 8000 K. Excellent agreement exists with the spectrophotometry and Balmer line profiles of Vega. A small systematic error in the colors of late A and F stars is probably due to an overestimate of convection in weakly convective models. This error does not seem to affect greatly the use of the predicted colors for differential studies. The solar model has approximately a 2% error in the V flux because molecular lines were not included.

Subject headings: spectrophotometry — stars: atmospheres — stars: early-type — Sun: atmosphere

I. INTRODUCTION

Several areas in model atmosphere research require intensive effort at the present time. Among these are the inclusion of realistic opacities, especially line opacity, the treatment of gas-radiation equilibrium (non-LTE), and the treatment of convection. We are not able to treat convection rigorously, but for many stars the overall energy distribution and spectrum are not greatly affected by the dimensional formulation and arbitrary constants of the mixing-length theory now in use. Non-LTE is extremely important for very hot stars and for low-gravity stars even at low temperatures, but models for many stars do not require detailed equilibrium calculations except for the cores of strong lines. Opacities play a role in any model calculation, and for many stars the inclusion of realistic opacities is the major requirement for computing realistic models. Incorrect opacities lead to models that produce errors in the determination of all four parameters—effective temperature, gravity, abundance, and microturbulence.

The first few figures illustrate qualitatively the effects of opacity changes. Figure 1 shows the change in the temperature structure of a model as the ultraviolet opacity is increased. The increased opacity makes it more difficult for the model to radiate, so the model adjusts by increasing the temperature in optically thick layers to maintain constant energy flow. As the atmosphere becomes optically thin in the regions of increased opacity, it becomes too easy for

the model to radiate, so the model adjusts by lowering the temperature in the surface layers. The energy distribution and line profiles are affected considerably because they are determined by the temperature gradient. Figure 2 shows the resulting increase in the

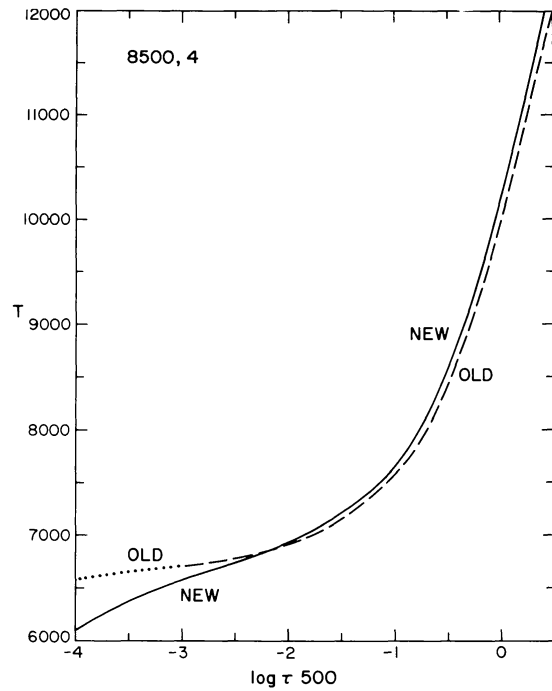


FIG. 1.—The effect of the T - τ relation of increasing the line opacity for an 8500, 4 model. The model labeled "new" has more opacity.

* Visiting Astronomer, Kitt Peak National Observatory, which is operated by the Association of Universities for Research in Astronomy, Inc., under contract with the National Science Foundation.

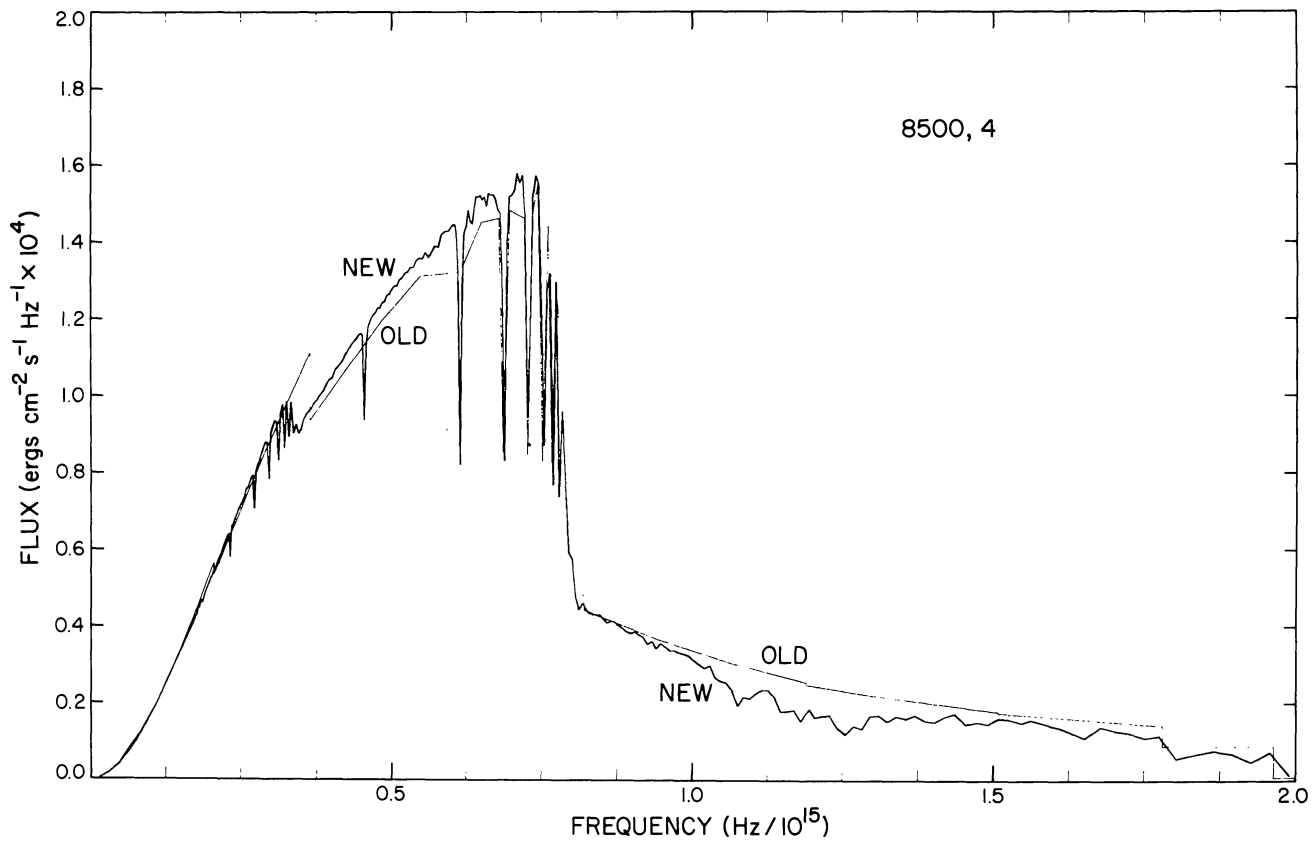


FIG. 2.—The effect on the flux F_v of increasing the line opacity for an 8500, 4 model

visible flux and slope, which makes up for the increased ultraviolet absorption. The area under the curves, the total flux, remains the same. An effective temperature determined from the visible color thus is sensitive to the opacity.

Figure 3 illustrates the effect on line profiles, specifically Balmer line profiles, which are used in gravity determinations. We see that the wings of the lines reflect the increased temperature gradient in the atmosphere and that the cores are deeper owing to

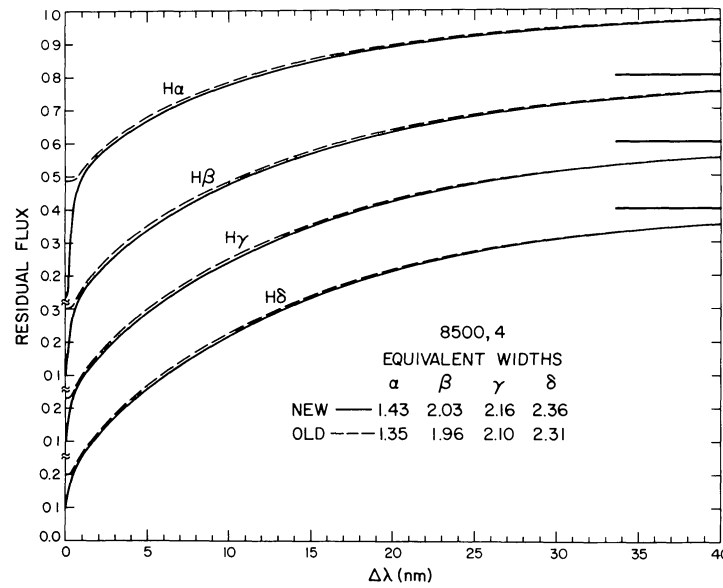


FIG. 3.—The effect on the Balmer line profiles of increasing the line opacity for an 8500, 4 model. The equivalent widths are given in nm.

the lower surface temperature. Depending on the model and the depth of formation, the line wings can be higher or lower and the equivalent widths of the lines can increase or decrease. In this case the lines are stronger. Thus the gravity determination from Balmer lines is sensitive to the opacity.

We find the same effects in the core and wings of metal lines: The equivalent width change affects the derived abundances and microturbulence. In the case where the core deepens and the wings rise, we have the curve of growth shown schematically in Figure 4. Since lines on the linear or flat part of the curve of growth do not have significant wings, the deeper core results in an increased equivalent width. Thus abundances derived from a model with too little opacity are systematically too large even for the weakest lines. Abundances for lines on the flat part of the curve of growth can be overestimated by large factors. The equivalent width of a line on the flat part of the curve of growth in a real star would be interpreted using an incorrect model as an indication of a high microturbulent velocity. The models presented in this paper are not perfect, so they too introduce such systematic errors, although, it is hoped, at a much lower level.

Since there are systematic errors in model atmospheres, the only safe strategy for determining abundances is, first, to choose a model that matches the observed energy distribution of the star (in the visible for lines in the visible). This model will have approximately the correct temperature gradient in the region of the atmosphere where the weak lines are formed, although it may have the wrong effective temperature and may not be able to reproduce the profiles of the strong lines. Second, only lines on the linear part of

the curve of growth should be used. Abundances are not reliable for any class of stars so faint that its weak lines have not yet been measured. Once abundances have been determined at high resolution, it may be possible to correlate them with features visible through lower-resolution spectra or photometry.

In this paper we use a statistical distribution-function representation for the opacity of atomic lines. We have computed distribution functions for abundances 10, 3, 1, 1/3, 1/10, 1/30, and 1/100 times solar and, thus far, models, fluxes, Balmer line profiles, and colors for solar and 1/10 and 1/100 times solar abundances. We discuss the distribution functions in a general way in § II and give computational details in § III. The model calculations are discussed in § IV. Section V discusses fluxes and Balmer line profiles and compares the calculations to observations. Colors and bolometric corrections are given in § VI. In § VII we compare our results with other grids of models. Next follow the tables of models, fluxes, Balmer line profiles, and colors. Finally, in an Appendix, we tabulate Rosseland mean opacities computed from the distribution functions. The colors are compared to observations in separate papers by Relyea and Kurucz (1978) and Buser and Kurucz (1978).

II. DISTRIBUTION FUNCTIONS FOR LINE OPACITY

The rationale for a statistical treatment of opacity is that the structure of a stellar atmosphere depends on integrals of the radiation field over frequency, such as the total flux at each depth, not on monochromatic quantities. Thus it might be expected that a statistical representation that removes the small-scale frequency

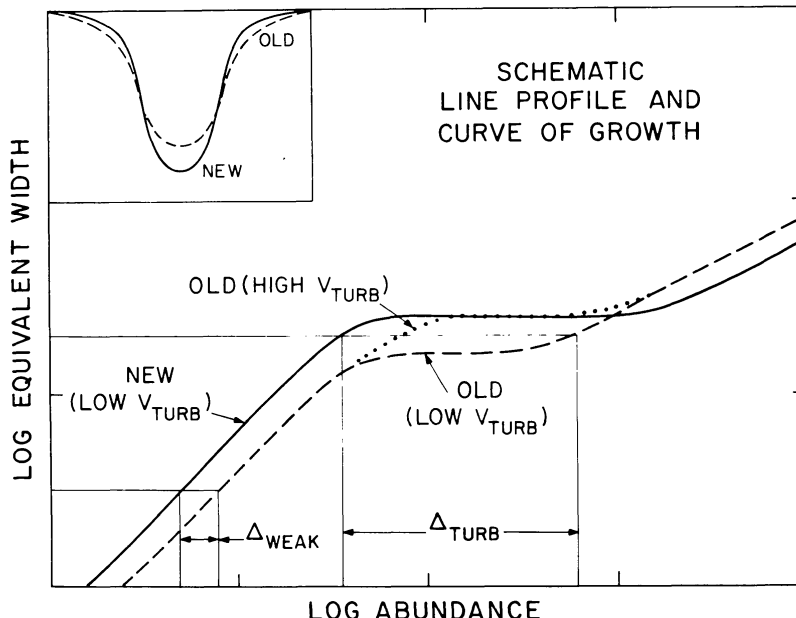


FIG. 4.—A schematic line profile and curve of growth, assuming no ionization changes, showing the effect of increasing the line opacity in the model atmosphere. For a given observed equivalent width, the new model predicts an abundance lower by Δ_{weak} for a weak line. For a line on the flat, microturbulently broadened part of the curve of growth, the new model predicts either an abundance lower by Δ_{weak} and a lower microturbulent velocity, or an abundance lower by Δ_{turb} with the same microturbulent velocity.

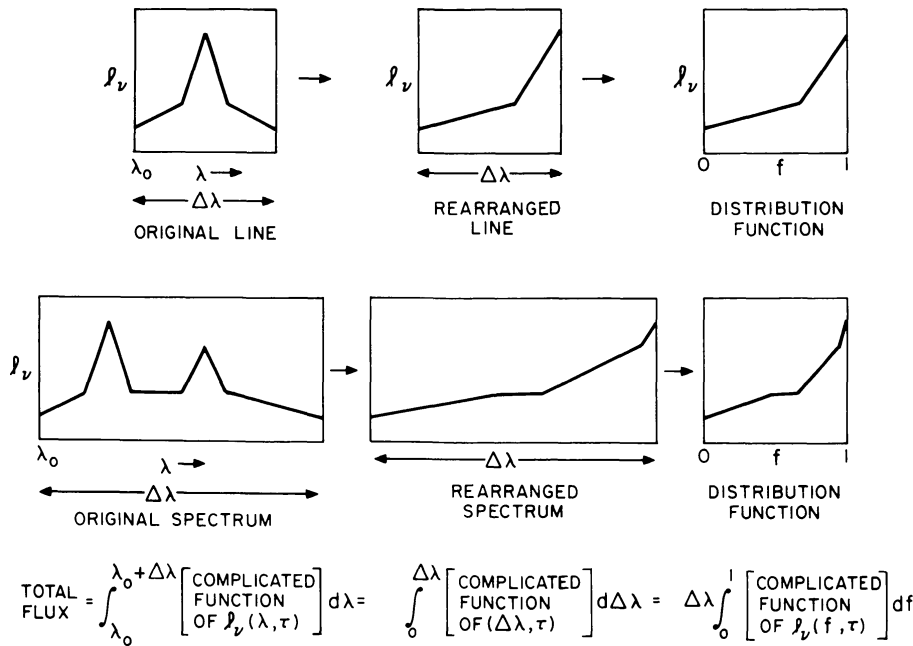


FIG. 5.—Schematic distribution functions. See text.

dependence of the opacity would, to a first approximation, not affect the integrals and would therefore be adequate for calculating model atmospheres. We can illustrate this with the simple example of a distribution-function representation for a single line profile. In Figure 5 we show the original absorption-coefficient profile and a new profile where the wavelength of each $d\lambda$ of the original profile has been discarded and the $d\lambda$'s have been rearranged so that l_ν is an increasing function. The rearranged profile produces the same total flux as the original. If we then normalize the length of the interval to 1, we obtain a distribution function that determines the fraction of the interval that has opacity l_ν or less. Integrating over the distribution function also produces the same total flux. If we treat a complicated spectrum in the same way, the distribution function is no more complicated computationally than that for a single line.

In representing line opacity by distribution functions, we make two implicit physical assumptions. The first is that the absorption-coefficient spectrum has the same relative shape at all depths in the atmosphere where line opacity is important as shown in Figure 6. These two cases have identical distribution functions at each depth. In Figure 6b the distribution function predicts the wrong optical depths because it assumes that the highest opacities always occur at the same frequencies. One way to investigate this effect is to compare distribution-function calculations to explicit line calculations. For example, see Carbon's (1974) discussion of distribution functions in his treatment of molecular opacity. Gustafsson *et al.* (1975) showed that this assumption did not produce a significant error in their models.

The second assumption is that either lines of different strengths are uniformly distributed through-

out the interval or the continuum source function and opacity do not vary radically over the frequency interval to which the distribution function applies, so that it makes no difference where in the interval the lines appear. If the interval for the distribution function is chosen such that strong opacity discontinuities are avoided, we obtain reasonably accurate results when the width of the interval is such that $\Delta\nu/\nu \lesssim 5-10\%$.

In practice, the spectrum is divided into a number of wavelength intervals and the distribution function is tabulated for a range of temperature, electron number or gas pressure, abundance, and micro-turbulent velocity. Figure 7 shows a wavelength

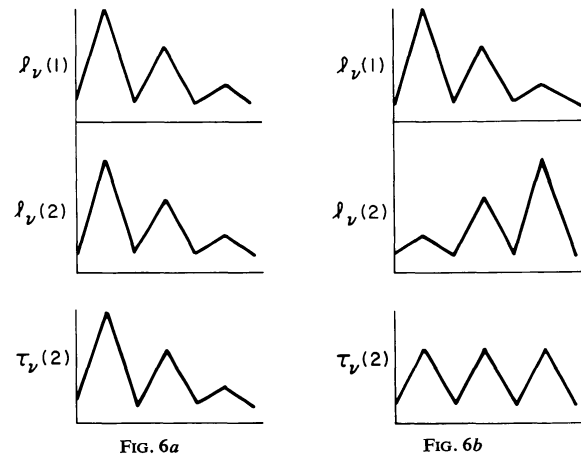


FIG. 6.—Schematic line absorption coefficient spectra at two depths. The distribution functions for Figs. 6a and 6b are identical at each depth, but the distribution functions for Fig. 6b would predict the wrong optical depth scale and the wrong radiation field.

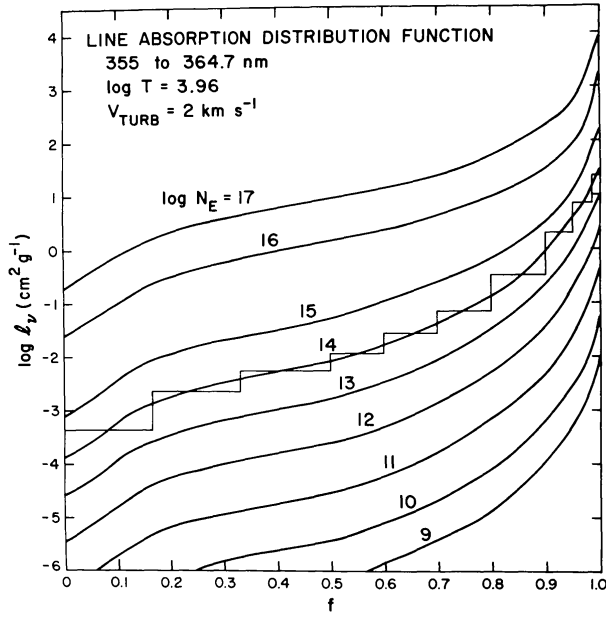


FIG. 7.—Sample distribution functions for a wavelength region just below the Balmer discontinuity for one temperature and nine values of electron number density. In practice, the distribution functions are represented by step functions, as indicated on the curve for $\log N_e = 14$.

region just below the Balmer discontinuity for one temperature and nine values of the electron density. Note how, as the density decreases, the maximum, which represents line cores, decreases owing to ionization, and how the wings decrease even more as the broadening is reduced at low densities. Computationally, the distribution functions can be represented by step functions, as indicated on the curve for $N_e = 14$. For each step i , the total opacity for each level of the atmosphere, the optical depth, the source function, and the radiation moments are evaluated as follows:

$$\tau_{vi} = \int_0^M (\kappa_v + \sigma_v + l_{vi}) dM, \quad (1)$$

$$S_{vi} = (\kappa_v \bar{S}_v + l_{vi} B_v + \sigma_v J_{vi}) / (\kappa_v + l_{vi} + \sigma_v), \quad (2)$$

$$J_{vi} = \frac{1}{2} \int_0^{\tau_{vi}} S_{vi} E_1(\tau_{vi} - t) dt + \frac{1}{2} \int_{\tau_{vi}}^{\infty} S_{vi} E_1(t - \tau_{vi}) dt, \quad (3)$$

$$H_{vi} = -\frac{1}{2} \int_0^{\tau_{vi}} S_{vi} E_2(\tau_{vi} - t) dt + \frac{1}{2} \int_{\tau_{vi}}^{\infty} S_{vi} E_2(t - \tau_{vi}) dt, \quad (4)$$

and

$$K_{vi} = \frac{1}{2} \int_0^{\tau_{vi}} S_{vi} E_3(\tau_{vi} - t) dt + \frac{1}{2} \int_{\tau_{vi}}^{\infty} S_{vi} E_3(t - \tau_{vi}) dt, \quad (5)$$

where M is the mass per unit area, κ_v and σ_v are the

continuous absorption and scattering coefficients, J_{vi} is the line absorption coefficient of the step, τ_{vi} is the optical depth, B_v is the Planck function, \bar{S}_v is the continuum source function, S_{vi} is the source function, J_{vi} is the mean intensity, H_{vi} is the flux moment, and K_{vi} is the pressure moment. Monochromatic quantities are found by integrating over the distribution function through simple addition of the steps,

$$J_v = \int_0^1 J_v(f_v) df_v = \sum_{i=1}^{N_v} w_{vi} J_{vi}, \quad (6)$$

$$H_v = \int_0^1 H_v(f_v) df_v = \sum_{i=1}^{N_v} w_{vi} H_{vi}, \quad (7)$$

and

$$K_v = \int_0^1 K_v(f_v) df_v = \sum_{i=1}^{N_v} w_{vi} K_{vi}, \quad (8)$$

where w_{vi} is the width of step i .

III. DISTRIBUTION FUNCTIONS FOR THIS GRID

The opacity calculation by Kurucz, Peytremann, and Avrett (1974, hereafter KPA) has been repeated with several significant improvements. First, the temperature range has been extended to cooler temperatures and a closer spacing has been adopted to improve the accuracy of interpolation from the final tables. The temperatures are listed in Table 1. Second, the state variable was changed from pressure to electron number, also listed in Table 1. This change has the great computational advantage that the metal line opacity scales with abundance at a given temperature and electron number, for fixed hydrogen and helium abundance, so that only one calculation is

TABLE 1
TABULATED TEMPERATURES AND ELECTRON NUMBER DENSITIES

| $\log T$ | $\log N_e$ | | | | | | | | |
|----------|------------|----|----|----|----|----|----|----|---|
| | 17 | 16 | 15 | 14 | 13 | 12 | 11 | 10 | 9 |
| 3.48 | | | | | | | x | x | x |
| 3.52 | | | | | | x | x | x | x |
| 3.56 | | | | | x | x | x | x | x |
| 3.60 | | | | x | x | x | x | x | x |
| 3.64 | | | x | x | x | x | x | x | x |
| 3.68 | | x | x | x | x | x | x | x | x |
| 3.72 | x | x | x | x | x | x | x | x | x |
| 3.76 | x | x | x | x | x | x | x | x | x |
| 3.80 | x | x | x | x | x | x | x | x | x |
| 3.84 | x | x | x | x | x | x | x | x | x |
| 3.88 | x | x | x | x | x | x | x | x | x |
| 3.92 | x | x | x | x | x | x | x | x | x |
| 3.96 | x | x | x | x | x | x | x | x | x |
| 4.00 | x | x | x | x | x | x | x | x | x |
| 4.10 | x | x | x | x | x | x | x | x | x |
| 4.20 | x | x | x | x | x | x | x | x | x |
| 4.30 | x | x | x | x | x | x | x | x | x |
| 4.40 | x | x | x | x | x | x | x | x | x |
| 4.50 | x | x | x | x | x | x | x | x | x |
| 4.60 | x | x | x | x | x | x | x | x | x |
| 4.70 | x | x | x | x | x | x | x | x | x |
| 4.80 | x | x | x | x | x | x | x | x | x |
| 4.90 | x | x | x | x | x | x | x | x | x |
| 5.00 | x | x | x | | | | | | |

TABLE 2
FREQUENCY INTERVALS

| Integration Wavelength | Distribution Function | | Integration Wavelength | Distribution Function | |
|------------------------|-----------------------|------------------|------------------------|-----------------------|--|
| | Interval | Subintervals | | Interval | Subintervals |
| 22.9 | 22.79409 | 23.2 | 230. | 225. | 227.5 230. 232.5 |
| 23.4 | | | 240. | 235. | 237.5 240. 242.5 |
| 24.3 | 23.65221 | | 248.1 | 245. | 247.5 250. |
| 25.2 | 25.00744 | 25.46614 | 258.1 | 251.38152 | 252.5 255. 257.5 260. 262.5 |
| 25.6 | | | 270. | 265. | 267.5 270. 272.5 |
| 26.0 | 25.90000 | 26.14316 | 280. | 275. | 277.5 280. 282.5 |
| 26.6 | | | 290. | 285. | 287.5 290. 292.5 |
| 27.5 | 27.1 | 28.09263 | 300. | 295. | 297.5 300. 302.5 |
| 28.3 | | | 310. | 305. | 307.5 310. 312.5 |
| 29.3 | 28.65871 | | 320. | 315. | 317.5 320. 322.5 |
| 30.1 | 29.95849 | 30.26260 | 330. | 325. | 327.5 330. 332.5 |
| 30.9 | | | 340. | 335. | 337.5 340. 342.5 |
| 32.5 | 31.7 | | 350. | 345. | 347.5 350. 352.5 |
| 34.2 | 33.5 | 34.96998 | 359.8 | 355. | 357.5 360. 362.5 |
| 35.1 | | | 366.1 | 364.70552 | 367.5 370. 372.5 |
| 35.6 | 35.25000 | 36.14101 | 368.7 | | |
| 36.5 | | | 371.2 | | |
| 37.5 | 37. | 38.01600 | 373.7 | | |
| 38.4 | | | 380. | 375. | 377.5 380. 382.5 |
| 40. | 38.96642 | | 390. | 385. | 387.5 390. 392.5 |
| 41.5 | 41.15492 | 41.879 | 402.5 | 395. | 397.5 400. 402.5 405. 407.5 |
| 42.5 | | | 420. | 410. | 412.5 415. 417.5 420. 422.5 425. 427.5 |
| 44.5 | 43.3 | | 440. | 430. | 432.5 435. 437.5 440. 442.5 445. 447.5 |
| 47.2 | 45.9 | | 460. | 450. | 452.5 455. 457.5 460. 462.5 465. 467.5 |
| 49.4 | 48.52000 | | 480. | 470. | 472.5 475. 477.5 480. 482.5 485. 487.5 |
| 50.6 | 50.43022 | 50.876 | 500. | 490. | 492.5 495. 497.5 500. 505. |
| 51.6 | | | 520. | 510. | 515. 520. 525. |
| 54. | 52.5 | | 540. | 530. | 535. 540. 545. |
| 56.4 | 55.5 | | 560. | 550. | 555. 560. 565. |
| 58.7 | 57.41000 | | 580. | 570. | 575. 580. 585. |
| 61.2 | 60. | | 605. | 590. | 595. 600. 605. 610. 615. |
| 64.0 | 62.5 | | 635. | 620. | 625. 630. 635. 640. 645. |
| 67.1 | 65.53786 | | 665. | 650. | 655. 660. 665. 670. 675. |
| 70.5 | 68.8 | | 695. | 680. | 685. 690. 695. 700. 705. |
| 73.6 | 72.24011 | | 730. | 710. | 720. 730. 740. |
| 77. | 75. | | 770. | 750. | 760. 770. 780. |
| 81. | 79. | | 805.2 | 790. | 800. 810. |
| 85. | 83. | | 835.2 | 820.58743 | 830. 840. |
| 89. | 87. | | 875. | 850. | 860. 870. 880. 890. |
| 93. | 91.17638 | 93. | 925. | 900. | 910. 920. 930. 940. |
| 97.5 | 95. | 97.5 | 975. | 950. | 960. 970. 980. 990. |
| 102.5 | 100. | 102.5 | 1025. | 1000. | 1010. 1020. 1030. 1040. |
| 107.5 | 105. | 107.5 | 1075. | 1050. | 1060. 1070. 1080. 1090. |
| 112.5 | 110.09203 | 112.5 | 1125. | 1100. | 1110. 1120. 1130. 1140. |
| 117.5 | 115. | 117.5 | 1175. | 1150. | 1160. 1170. 1180. 1190. |
| 121.9 | 120. | 122. | 1225. | 1200. | 1210. 1220. 1230. 1240. |
| 126.9 | 123.96176 | 127. | 1275. | 1250. | 1260. 1270. 1280. 1290. |
| 132.5 | 130. | 132.5 | 1325. | 1300. | 1310. 1320. 1330. 1340. |
| 137.5 | 135. | 137.5 | 1375. | 1350. | 1360. 1370. 1380. 1390. |
| 142.2 | 140. | 142.2 | 1429.4 | 1400. | 1410. 1420. 1430. 1440. 1450. |
| 148.2 | 144.40176 | 147. 149.5 | 1479.4 | 1458.82209 | 1470. 1480. 1490. |
| 154.5 | 152.00002 | 154.5 | 1550. | 1500. | 1520. 1540. 1560. 1580. |
| 159.5 | 157. | 159.5 | 1650. | 1600. | 1620. 1640. 1660. 1680. |
| 164.9 | 162.15071 | 165. | 1675. | | |
| 171.3 | 167.67209 | 170. 172.5 | 1800. | | |
| 179. | 175. | 177.5 180. | 2700. | | |
| 187. | 183. | 185. 187.5 | 4000. | | |
| 194.4 | 191. | 193. 195. | 5000. | | |
| 202.8 | 197.84471 | 200. 202.5 205. | 6500. | | |
| 211.3 | 207.75641 | 210. 212.5 | 10000. | | |
| 220. | 215. | 217.5 220. 222.5 | 20000. | | |

needed to determine the distribution function for all abundances. Hydrogen and helium must remain fixed because they are the van der Waals perturbers that broaden the strong lines. Unfortunately, in regions where hydrogen or helium lines provide the dominant opacity, scaling does not work, so those regions must be recalculated when the metal abundances are changed. In practice, we recalculated only for wavelength intervals having the hydrogen Lyman, Balmer, Paschen, and Brackett lines as indicated in Table 2.

We did not directly evaluate the distribution function at every value of T and N_e since many of the combinations would not occur in the model atmos-

spheres, namely, high temperatures at low densities and low temperatures at high densities. Table 1 indicates the values at which the calculations were performed. To simplify interpolation, the distribution-function tables have been filled out by logarithmic linear extrapolation.

One change was made in the adopted solar abundances: iron was increased from -4.65 to -4.50 relative to the total number of atoms, which we prefer from our own experiments with weak lines. The adopted solar abundances taken from Withbroe's (1971) compilation or Allen (1963) are listed in Table 3. The values listed are logarithmic abundances relative

to the total. We assumed 0.9 hydrogen and 0.1 helium by number in all these calculations.

The final important change in the distribution-function calculation was to improve the wavelength resolution by modifying the program to calculate simultaneously distribution functions for a large wavelength interval and for smaller subintervals. Thus two sets of distribution functions were tabulated, one with nominally 10 nm intervals to be used to calculate the models, and a second with nominally 2.5 nm intervals to be used to calculate surface fluxes once the models had converged. The higher resolution is needed to calculate intermediate-band colors. The wavelength intervals are listed in Table 2. Since the Balmer discontinuity is such a dominant feature in stars, the smaller intervals in the region 365–375 nm were used in both sets to improve integration across the discontinuity. For wavelengths longward of the last interval, the last interval was assumed to extend to infinity.

For line data we used the list computed by Kurucz and Peytremann (1975). To simplify the calculation, the data were edited down to fewer than 1,000,000 lines from the original 1,760,000 by eliminating lines with gf -values less than 10^{-5} when the lower energy level was greater than $15,000 Z_{\text{eff}} \text{ cm}^{-1}$, where Z_{eff} (the effective charge) is 1 for neutrals, 2 for once ionized atoms, etc. We have assumed that the summed opacity

of the deleted lines is insignificant, but we have not been able to test the assumption, as it would require recomputing the distribution function. A magnetic tape containing the line data can be obtained from the author.

We selected line data for each distribution-function interval slightly beyond both ends to be sure to pick up the wings of lines in neighboring intervals. There were between 15,000 and 30,000 lines per interval above the Lyman limit, with a falling off of the number in the Lyman continuum owing to a shortage of spectral information on multiply ionized atoms.

For each interval we calculated the total absorption coefficient at points evenly spaced in wavelength such that $\Delta\lambda/\lambda_{\text{center}} = 2.5E-6$, where λ_{center} is the center of the interval. This spacing produced several points per Doppler width in the Voigt profile of each line. To save time, we used a minimum cutoff of 1/1000 of the continuum opacity to limit the spread of the line wings. The wing opacity is due to radiative, van der Waals, and Stark broadening, which are approximated as follows in the present calculation:

A. The radiative damping constant is assumed equal to the classical damping constant:

$$\Gamma_R = 2.223E13/\lambda_{\text{center}}^2 \text{ (in s}^{-1}, \lambda \text{ in nm}) \quad (9)$$

(see the discussion by Peytremann 1972).

TABLE 3
ABUNDANCES

| Atomic Number | Element | Abundance | Atomic Number | Element | Abundance | Atomic Number | Element | Abundance |
|---------------|---------|-----------|---------------|---------|-----------|---------------|---------|-----------|
| 1..... | H | -0.05 | 34..... | Se | -8.80 | 67..... | Ho | -11.50 |
| 2..... | He | -1.00 | 35..... | Br | -9.40 | 68..... | Er | -11.29 |
| 3..... | Li | -11.45 | 36..... | Kr | -8.80 | 69..... | Tm | -11.62 |
| 4..... | Be | -10.99 | 37..... | Rb | -9.42 | 70..... | Yb | -11.24 |
| 5..... | B | -9.25 | 38..... | Sr | -9.23 | 71..... | Lu | -11.21 |
| 6..... | C | -3.48 | 39..... | Y | -10.43 | 72..... | Hf | -11.40 |
| 7..... | N | -3.99 | 40..... | Zr | -9.63 | 73..... | Ta | -11.70 |
| 8..... | O | -3.22 | 41..... | Nb | -9.75 | 74..... | W | -9.48 |
| 9..... | F | -7.49 | 42..... | Mo | -10.15 | 75..... | Re | -11.40 |
| 10..... | Ne | -4.60 | 43..... | Tc | -20.00 | 76..... | Os | -11.30 |
| 11..... | Na | -5.81 | 44..... | Ru | -10.48 | 77..... | Ir | -9.84 |
| 12..... | Mg | -4.51 | 45..... | Rh | -10.50 | 78..... | Pt | -10.40 |
| 13..... | Al | -5.65 | 46..... | Pd | -10.48 | 79..... | Au | -11.73 |
| 14..... | Si | -4.50 | 47..... | Ag | -11.38 | 80..... | Hg | -9.05 |
| 15..... | P | -6.62 | 48..... | Cd | -10.08 | 81..... | Tl | -11.85 |
| 16..... | S | -4.84 | 49..... | In | -10.34 | 82..... | Pb | -10.18 |
| 17..... | Cl | -6.40 | 50..... | Sn | -10.34 | 83..... | Bi | -11.25 |
| 18..... | Ar | -5.40 | 51..... | Sb | -10.40 | 84..... | Po | -20.00 |
| 19..... | K | -7.00 | 52..... | Te | -10.00 | 85..... | At | -20.00 |
| 20..... | Ca | -5.72 | 53..... | I | -10.60 | 86..... | Rn | -20.00 |
| 21..... | Sc | -8.98 | 54..... | Xe | -10.00 | 87..... | Fr | -20.00 |
| 22..... | Ti | -7.31 | 55..... | Cs | -10.90 | 88..... | Ra | -20.00 |
| 23..... | V | -7.95 | 56..... | Ba | -10.15 | 89..... | Ac | -20.00 |
| 24..... | Cr | -6.35 | 57..... | La | -10.24 | 90..... | Th | -11.23 |
| 25..... | Mn | -6.85 | 58..... | Ce | -10.41 | 91..... | Pa | -20.00 |
| 26..... | Fe | -4.50 | 59..... | Pr | -10.42 | 92..... | U | -11.45 |
| 27..... | Co | -7.55 | 60..... | Nd | -10.23 | 93..... | Np | -20.00 |
| 28..... | Ni | -5.77 | 61..... | Pm | -20.00 | 94..... | Pu | -20.00 |
| 29..... | Cu | -7.60 | 62..... | Sm | -10.39 | 95..... | Am | -20.00 |
| 30..... | Zn | -7.63 | 63..... | Eu | -11.56 | 96..... | Cm | -20.00 |
| 31..... | Ga | -9.21 | 64..... | Gd | -10.93 | 97..... | Bk | -20.00 |
| 32..... | Ge | -8.73 | 65..... | Tb | -11.60 | 98..... | Cf | -20.00 |
| 33..... | As | -9.70 | 66..... | Dy | -10.94 | 99..... | Es | -20.00 |

B. The van der Waals damping constant is approximated by

$$\Gamma_W = \frac{n_{\text{eff}}^2}{z_{\text{eff}}} 17 \left(\frac{8kT}{\pi M} \right)^{0.3} \times [(1.61E - 33)^{0.4} N_H + (\frac{1}{4})^{0.3} (0.50E - 33)^{0.4} N_{He}] \quad (s^{-1}), \quad (10)$$

where in the usual hydrogenic expression $[(n_{\text{eff}}^2/z_{\text{eff}})^2]^{0.4}$ has been replaced by $n_{\text{eff}}^2/z_{\text{eff}}$ and the mass has not been reduced (to save computation time). Here, n_{eff} is the effective quantum number of the upper energy level, z_{eff} is the effective charge, and N_H and N_{He} are hydrogen and helium number densities. This expression is probably an underestimate since multiplicative factors of 2–6 usually must be introduced to make calculated damping constants agree with observations.

C. The Stark damping constant is a fit by Peytermann to detailed calculations by Sahal-Bréchot and Segré (1971):

$$\Gamma_S = 1.0E - 8n_{\text{eff}}^5 N_e \quad (s^{-1}). \quad (11)$$

Hydrogen lines are added separately to the total line-absorption coefficient by using the approximate Stark-profile algorithm found in subroutines HLINOP and STARK of the model atmosphere program ATLAS (Kurucz 1970). A microturbulent velocity of 2 km s⁻¹ was adopted.

After the total line-absorption coefficient has been calculated for every wavelength point in the region, the fraction of the total number of points that fall below each 1/10 decade in opacity is determined. This distribution function is interpolated to yield the opacity at 60 evenly spaced points ($f = 1/120$ to $119/120$), forming a 60-step histogram.

In practice, fewer than 60 steps are required to represent the line opacity adequately, so several steps are averaged together to form wider ones. A table of the resulting step functions is written on tape for each interval for use in ATLAS. For this grid we have taken 10 steps: 10/60, 10/60, 10/60, 6/60, 6/60, 6/60, 6/60, 3/60, 2/60, and 1/60, as in Figure 7 for $\log N_e = 14$.

IV. MODELS

a) Model Atmosphere Program

Several modifications have been made to ATLAS (Kurucz 1970) in the course of this work, which include changes in the temperature correction, radiation pressure, convection, and distribution functions, and correction of some minor numerical instabilities and bugs.

In ATLAS5 (Kurucz 1970) the depth variable is mass per square centimeter and the flux temperature correction determines a mass perturbation that changes the temperature to reduce the flux error. However, the physical variable for the radiation field is an optical depth scale. At high temperature the mass and optical depth scales vary in a similar fashion be-

cause the gas is mostly ionized, but at lower temperatures the optical depth scale becomes a very strong function of temperature because of ionization and Boltzmann population changes. Thus the mass correction tends to be slowly convergent or even unstable. To correct this problem, the temperature correction was changed from a mass to an optical depth correction by replacing dM in the perturbation equations by using

$$dM = d\tau_{\text{Ross}} / \langle \kappa_\nu + l_\nu + \sigma_\nu \rangle_{\text{Ross}} \quad (12)$$

and perturbing for $\Delta\tau_{\text{Ross}}$ instead of ΔM , where M is the mass per unit area and τ_{Ross} is the Rosseland optical depth. Then

$$\Delta T = -\Delta\tau_{\text{Ross}} \frac{dT}{d\tau_{\text{Ross}}}. \quad (13)$$

However, for the τ correction to work, the model must be defined on a fixed τ scale. To accomplish this while using mass as the variable, we determine an additional mass correction ΔM that approximately maintains the same Rosseland depth scale from iteration to iteration. This is found through approximate integration of equation (12) before and after the temperature correction, using Rosseland opacity pretabulated as a function of temperature and pressure (see Appendix). Then

$$\Delta M = M(T) - M(T + \Delta T). \quad (14)$$

There are several implicit assumptions in ATLAS5 about the radiation energy density and pressure that in some cases can affect the thermodynamic derivatives that determine the adiabatic gradient and, consequently, the convective flux. These approximations are now made more explicitly so that they can be removed if necessary.

The radiation pressure and the partial derivatives

$$\left(\frac{\partial P_{\text{rad}}}{\partial T} \right)_P, \left(\frac{\partial P_{\text{rad}}}{\partial P} \right)_T, \left(\frac{\partial E_{\text{rad}}}{\partial T} \right)_P, \left(\frac{\partial E_{\text{rad}}}{\partial P} \right)_T$$

are required to evaluate the thermodynamic expressions, where

$$P_{\text{rad}} = \frac{4\pi}{c} \int K_\nu d\nu \quad (15)$$

and the energy density per unit mass is

$$E_{\text{rad}} = \frac{4\pi}{\rho c} \int J_\nu d\nu, \quad (16)$$

with ρ the mass density. In an isotropic medium $J_\nu = 3K_\nu$, so $E_{\text{rad}} = 3P_{\text{rad}}/\rho$. This approximation was used in ATLAS5 and in the models presented here. At the top of the atmosphere the approximation can be in error by as much as 25%; but as the energy density affects the model only through the convective flux and, in these models, the convection zone starts at depths that are becoming optically thick, this approximation should not cause significant errors.

We save time in computing the radiation pressure by integrating the radiative acceleration instead of computing K directly. Using

$$\frac{dK_v}{dM} = (\kappa_v + l_v + \sigma_v)H_v, \quad (17)$$

we have

$$P_{\text{rad}} = \int_0^M \frac{4\pi}{c} \int (\kappa_v + l_v + \tau_v)H_v dv dM + P_{\text{rad}}(0) \quad (18)$$

$$= \int_0^M a_{\text{rad}} dM + P_{\text{rad}}(0), \quad (19)$$

where

$$P_{\text{rad}}(0) = \frac{4\pi}{c} \int K_v(0) dv. \quad (20)$$

Here, P_{rad} is the radiation pressure and a_{rad} is the radiative acceleration. Since the constant $P_{\text{rad}}(0)$ does not affect the gas pressure found through integrating the hydrostatic equilibrium equation but only adds to the total pressure, it was taken to be 0 in ATLAS5. In the models presented here, $K_v(0)$ was computed and $P_{\text{rad}}(0)$ was included explicitly because the thermodynamic derivatives can be affected. Unfortunately, it is impractical to compute these derivatives rigorously by recomputing the radiation field, so various approximations still must be used. For the optically thick isotropic case the radiation pressure varies as T^4 and is independent of the gas pressure,

$$\left(\frac{\partial P_{\text{rad}}}{\partial T} \right)_P = \frac{4P_{\text{rad}}}{T} \quad (21)$$

and

$$\left(\frac{\partial P_{\text{rad}}}{\partial P} \right)_T = 0. \quad (22)$$

At the surface,

$$\left(\frac{\partial P_{\text{rad}}}{\partial T} \right)_P = 0 \quad (23)$$

because the radiation field is not affected by local conditions but is formed deeper in the atmosphere. An approximate interpolating formula is required between the two cases. In ATLAS5 we used

$$\left(\frac{\partial P_{\text{rad}}}{\partial T} \right)_P = \frac{4[P_{\text{rad}} - P_{\text{rad}}(0)]}{T}. \quad (24)$$

For these models we used

$$\left(\frac{\partial P_{\text{rad}}}{\partial T} \right)_P = \frac{4P_{\text{rad}}}{T} [1 - \exp(-\tau_{\text{Ross}})]. \quad (25)$$

We do not know whether either approximation is preferable.

Modifications were also made to ATLAS in the treatment of the opacity steps. Since the same step widths are used to fit the distribution functions at all wavelengths, even when line opacity does not fill the interval, an algorithm was adopted to delete superfluous steps. At each frequency the continuum opacity and radiation field are calculated and stored. Then the line opacity is read in and combined with the continuous opacity starting with the highest step. The radiation field is calculated for the step. If the residual flux at any depth is less than 0.999, i.e., the line opacity is significant, the calculation continues to the next step and the test is repeated. Otherwise, all succeeding, lesser steps are assumed to be continuum and so are not calculated. This procedure results in a considerable saving in computer time.

The new version of the program, called ATLAS6, includes the modifications described above and can be obtained from the author together with the distribution functions. Also available are the updated abundance analysis program WIDTH6 that determines the abundance required to match an observed equivalent width or calculates curves of growth and an ATLAS6 subroutine XLINOP that computes line opacity for up to 1000 atomic and molecular lines with provision for isotopes.

b) Grid of Models

The models were computed with the program ATLAS6 assuming plane-parallel geometry, hydrostatic equilibrium, local thermodynamic equilibrium, no molecules in the equation of state, and radiative plus convective energy transport. The mixing-length to scale-height ratio was assumed to be 2 instead of the usual 1–1.5 because our convective formulation tends to produce a lower convective flux than other formulations such as that of Mihalas (1970). The convective flux was always computed; but for hotter models where it was not significant, the models were assumed to be strictly radiative. Continuous opacities were included for H I and H II, He I–He III, C I–C IV, N II–N V, O II–O VI, Ne I–Ne VI, Mg I, Al I, Si I, H₂⁺, H⁻, H Rayleigh scattering, and electron scattering. Three sets of abundances were used: solar as given in Table 3, 1/10 times solar, and 1/100 times solar, where all elements but hydrogen and helium were reduced by a constant factor.

Forty mass depth points were chosen to have Rosseland optical depths running from approximately $\log \tau_{\text{Ross}} = -4.5$ to 2.0 with six points per decade. In depth integrals either the first depth point was taken to be 0 or the integrand was extrapolated to 0 depth. Frequency integrations used the 122 wavelengths listed in Table 2 with trapezoidal integration in frequency. At 0 frequency and at the frequency corresponding to 22.4 nm there was assumed to be no radiation. For cooler models the Lyman continuum emits so little radiation that it was ignored without affecting the integrals.

Radiative models were converged to flux errors of a few tenths of a percent and flux derivatives to the

order of 1%, except at the top few points where the derivative was left on the order of 10%. The convective models were very slowly convergent and had flux errors in the convective zone, which, in some cases, were as large as 3% with alternating signs. In all cases the flux correction was reduced to a few tenths of a degree and the temperature structure and radiation field were converged, except at the first few points where there is a large temperature drop.

The model atmospheres are presented in Table 4 (see pages 31 and 33). A list of the models is given in Table 5 (see pages 31 and 175). There are 140 solar abundance models ranging in effective temperature from 5500 to 50,000 K computed at steps of 0.5 in $\log g$ down to the radiation pressure limit. A model 0.5 lower in $\log g$ than the lowest gravity model given cannot be computed in hydrostatic equilibrium. Also included are a solar model and models for Vega, which will be described in § VI. The 1/10 and 1/100 times solar abundance models were computed only for a limited range of six gravities for temperatures from 5500 to 10,000 K.

To compress the tables as much as possible, all quantities except temperature are given in log cgs units. The columns are mass cm^{-2} , Rosseland optical depth, continuum optical depth at 500 nm, geometric depth down from the first point, temperature, gas pressure, electron number density, atomic number density, mass density, Rosseland mass absorption coefficient, continuum mass absorption coefficient at 500 nm, radiation pressure, radiative acceleration (compare to $\log g$), and the fraction of the total flux carried by convection. A value of 0 in the table means an actual 0, not 10⁰. A label in the heading for each model tells whether the model was treated as purely radiative or radiative plus convective. The 40 depths listed in the table are the actual depths that were used in the calculation.

These models are available on tape or cards from the author.

c) Discussion

We experienced no significant numerical problems, and these models are as good as, or, in most cases, significantly better than earlier work, as discussed in § VII. Nevertheless, we expect to include improvements to our numerical procedures in future calculations. In the current grid we do not go to shallow enough optical depths to compute the temperature drop at the surface accurately. Test calculations with 99 depths indicate that a good approximation to the actual behavior at small depths can be found by linearly extrapolating the temperature from the third and fourth points to shallower depths. We plan to use 64 depths in future calculations going to at least $\log \tau_{\text{Ross}} = -6$ and adding more points per decade.

Several ATLAS users have pointed out that our integration for the radiation field (Kurucz 1970) assumes a smooth source function variation at small depths, which is not the case if there is a temperature drop. In future calculations we plan to add additional

shallow optical depths to the integration. We expect this change to improve the convergence of the flux derivative.

The addition of more points per decade should improve the evaluation of the derivatives in the convection zone and improve convergence of the convective flux. In any case our treatment of convection is uncertain. Once we are able to make detailed comparisons to observations, especially at the H⁻ opacity minimum at 1.64 μm , where the convective layers of an atmosphere are visible for some stars, we may adopt another mixing length, or another convective formulation altogether.

We computed a $T_{\text{eff}} = 10,000$ K, $\log g = 4$ test model using all the wavelengths given in Table 6 (see pages 31 and 184), which are 3 times as many as those used in this grid calculation. We did not find a significant difference in the models. However, we do expect that additional wavelengths are required in the far-ultraviolet for high-temperature models where the flux peaks in the ultraviolet. Also, the cooler models, especially once molecules are included, will probably require more wavelengths.

The cooler models in this grid should be recomputed with molecules in the equation of state and with molecular line opacities. We are currently making up a list of the required diatomic molecular lines.

In using the lowest-gravity models, the reader should consider that our assumptions of plane-parallelism, hydrostatic equilibrium, and LTE become less realistic.

V. FLUXES, COLORS, BOLOMETRIC CORRECTIONS, AND BALMER LINE PROFILES

a) Fluxes

Once the models were converged using the wavelengths listed in Table 2, the surface flux was computed at higher resolution at the wavelengths given in Table 6. That table lists flux per unit wavelength, $F_{\lambda}(=4H_{\lambda})$, and blocking fractions, which are 1 minus the ratio of the actual flux to the continuum flux in each wavelength interval. These data are available on magnetic tape from the author.

Figures 8–20 present an overall impression of the solar abundance models. Figures 8–13 present F_{ν} on a linear scale to show the relative contributions to the flux integral as the temperature increases from 6000 to 25,000 K and the flux maximum moves to the ultraviolet. Note that our resolution is high enough to show the hydrogen lines: L α at 2.5×10^{15} , the Balmer series from 0.25 to 0.8×10^{15} , and the Paschen series from 0.25 to 0.4×10^{15} Hz. The Lyman, Balmer, and Paschen discontinuities are apparent at 3.3, 0.8, and 0.4×10^{15} Hz, respectively. The strong line absorption in the Balmer continuum is apparent.

Figures 14–18 show $\log F_{\nu}$ and $\log F_{\lambda}$ for most of the $\log g = 4$ models for the ultraviolet wavelength and frequency intervals observable from space and for intervals observable from the ground.

Figure 19 shows the visible colors of most of the $\log g = 4$ models. These are magnitudes normalized

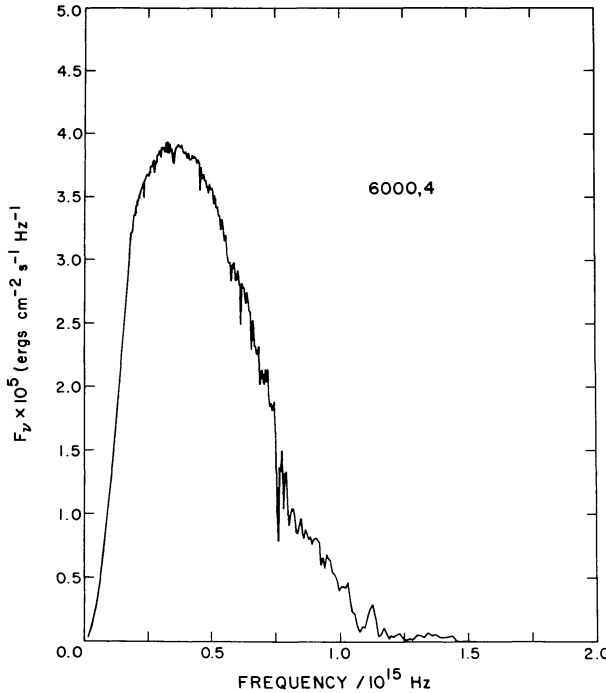


FIG. 8.—Flux F_ν for the 6000, 4 solar abundance model. In Figs. 8–13, the increased flux in the Balmer continuum and the shift of the flux maximum to the ultraviolet should be noted. As the temperature increases, the Paschen, Balmer, and Lyman discontinuities become visible, as well as individual Paschen, Balmer, and Lyman lines.

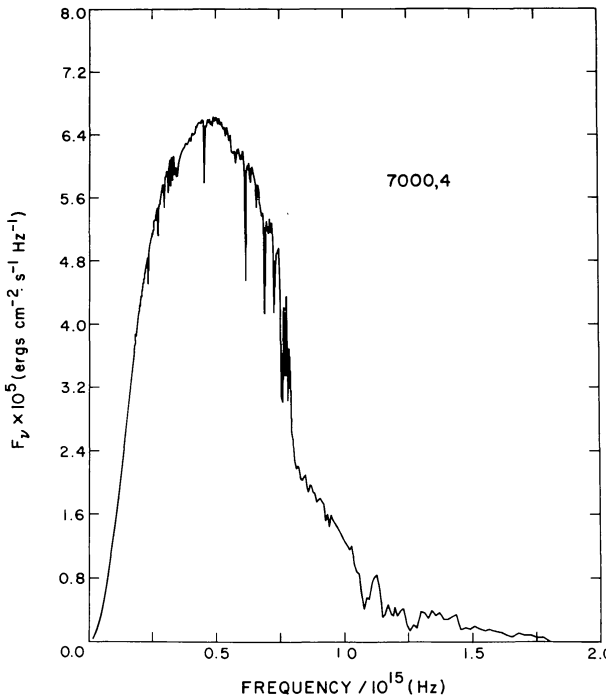


FIG. 9.—Same as Fig. 8 for 7000, 4

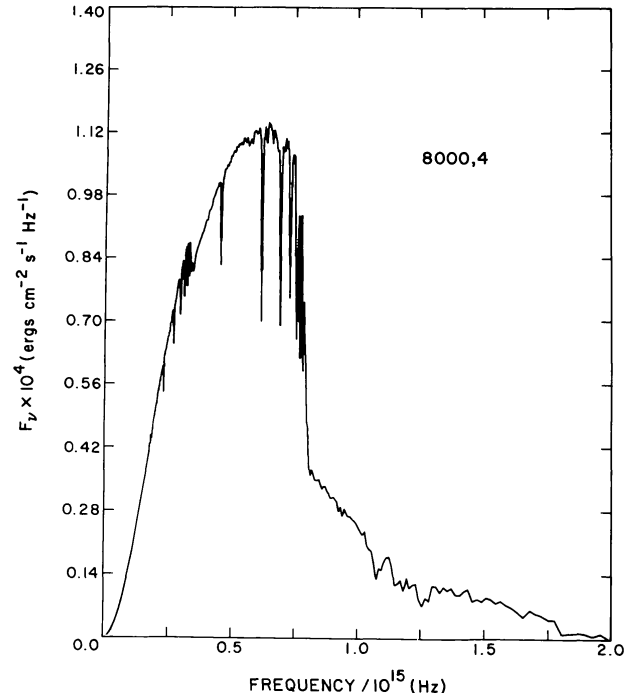


FIG. 10.—Same as Fig. 8 for 8000, 4

at $1.8 \mu\text{m}^{-1}$, the approximate position of the V filter. The dramatic change in the Balmer continuum relative to V as the temperature increases is obvious, as are the change in color in the visible and the limiting color in the infrared, visible, and ultraviolet at high temperatures.

Finally, Figure 20 shows F_ν over the whole frequency range for the hottest models for both the lowest and the highest-gravity model computed. Note the Balmer limit at 0.8×10^{15} , the Lyman limit at 3.3×10^{15} , the He I limit at 6.0×10^{15} , and the He II limit at $13.0 \times 10^{15} \text{ Hz}$. A strong effect on the energy distribution is apparent in the 35,000 K models above and below the Lyman limit as the gravity is reduced. This results from ionizing He I and removing its opacity, thereby reducing the temperature gradient.

b) Colors and Bolometric Corrections

Schild, Peterson, and Oke (1971) were able to match the energy distribution for Vega observed by Oke and Schild (1970) with a model that included line opacity only for hydrogen. However, KPA could not match the energy distribution with models that included a more realistic opacity. Because of this discrepancy, KPA were not able to calibrate their UBV colors by transforming the theoretical colors for Vega to match the observed colors but, instead, adopted the color calibration of Matthews and Sandage (1963). Furthermore, there was an artifact in the computed energy distribution for the 8000 and 8500 K models just to the red of the Balmer discontinuity that could contaminate the U magnitude, which caused KPA concern about the accuracy of the

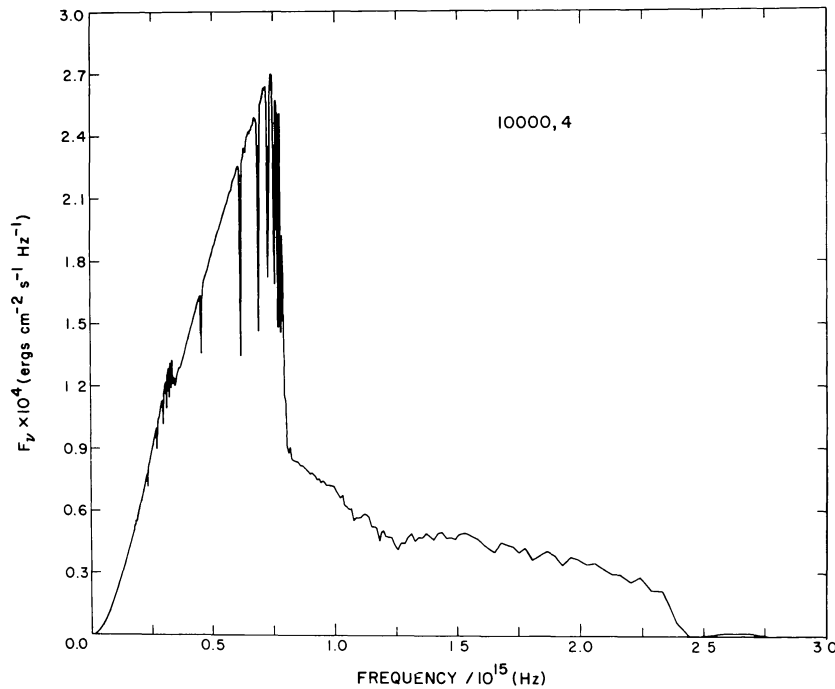


FIG. 11.—Same as Fig. 8 for 10,000, 4

model calculation. However, they decided that since only a few of their lowest-temperature models were affected, there would not be serious problems with the grid as a whole.

Systematic errors have been found in the *UBV* colors predicted by KPA: up to -0.05 in $B - V$ and up to -0.20 in $U - B$. An investigation of the difficulties encountered by KPA and of the errors in the colors led to the identification of three separate problems that have been corrected or, at least, substantially reduced in this work.

First, the Oke and Schild calibration for Vega has been revised. Careful reading of their paper and one by Hayes (1970) and conversations with Drs. Schild, Hayes, and Latham identified a number of possible systematic errors. Hayes and Latham (1975) made a careful rereduction of the Oke and Schild (1970) and Hayes (1970) Vega observations and included new infrared observations by Hayes, Latham, and Hayes (1975). They confirmed the existence of systematic errors, especially in the treatment of the extinction, and they reduced those errors to produce an improved

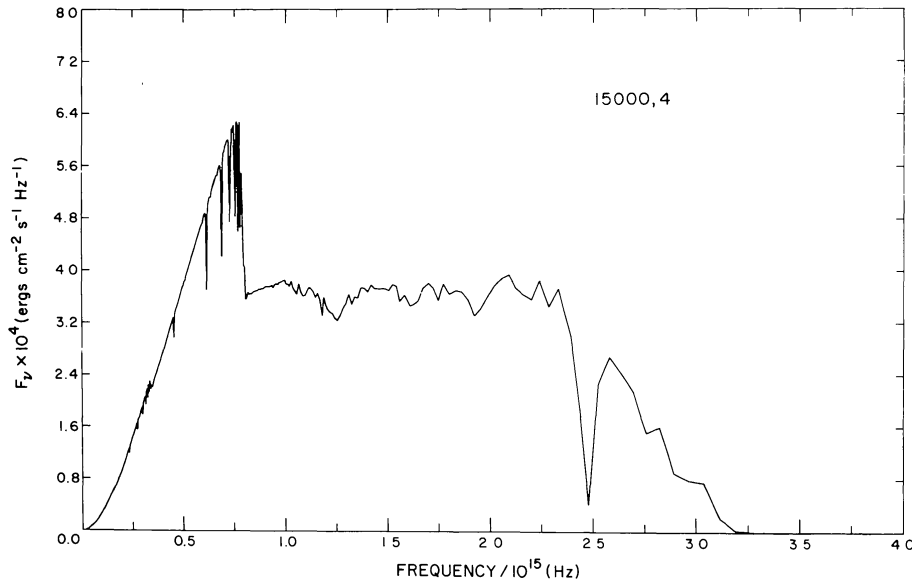


FIG. 12.—Same as Fig. 8 for 15,000, 4

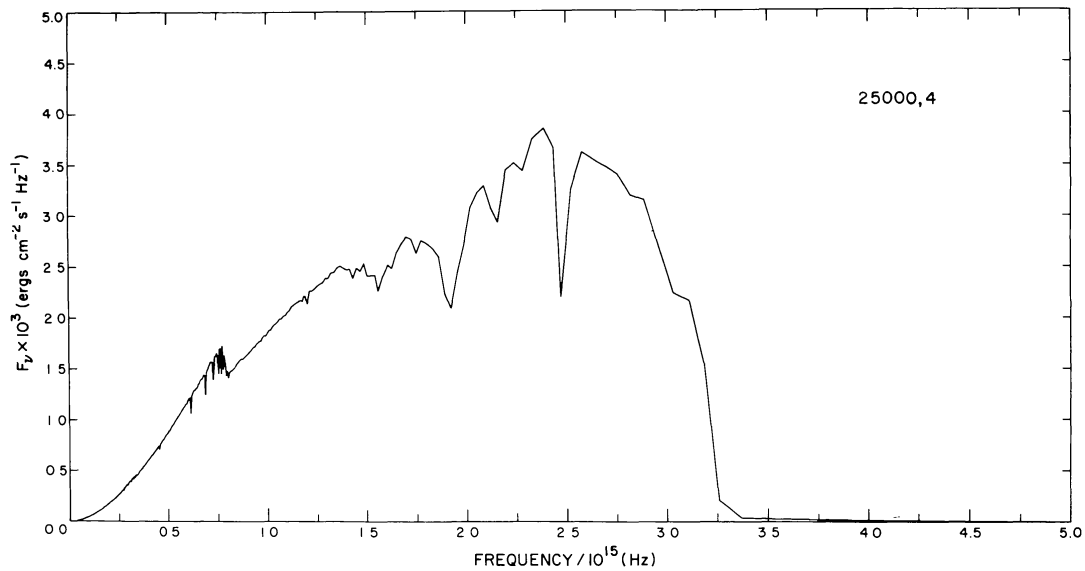
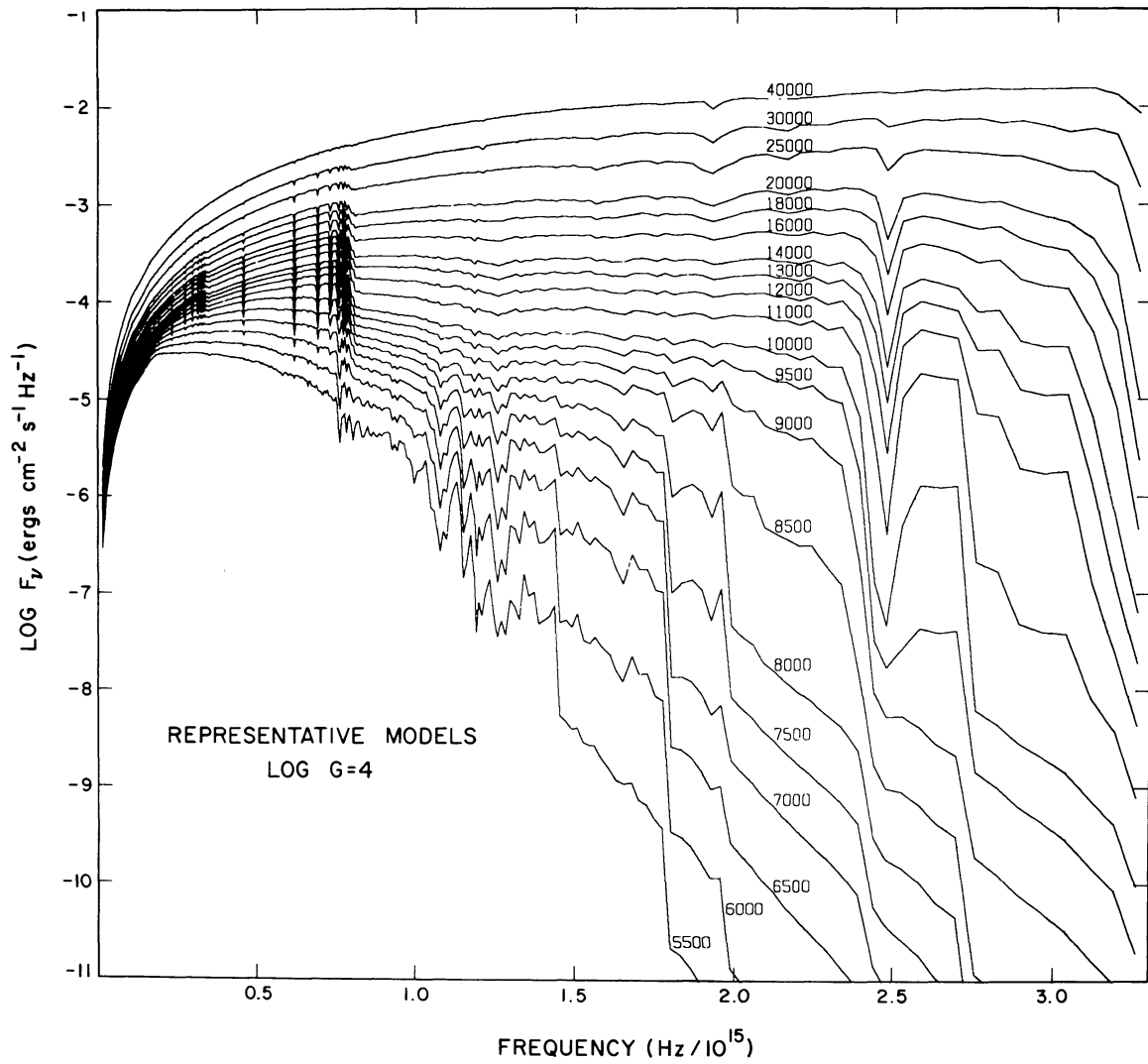


FIG. 13.—Same as Fig. 8 for 25,000, 4

FIG. 14.—The flux F_ν redward of the Lyman limit as a function of effective temperature for solar abundance models

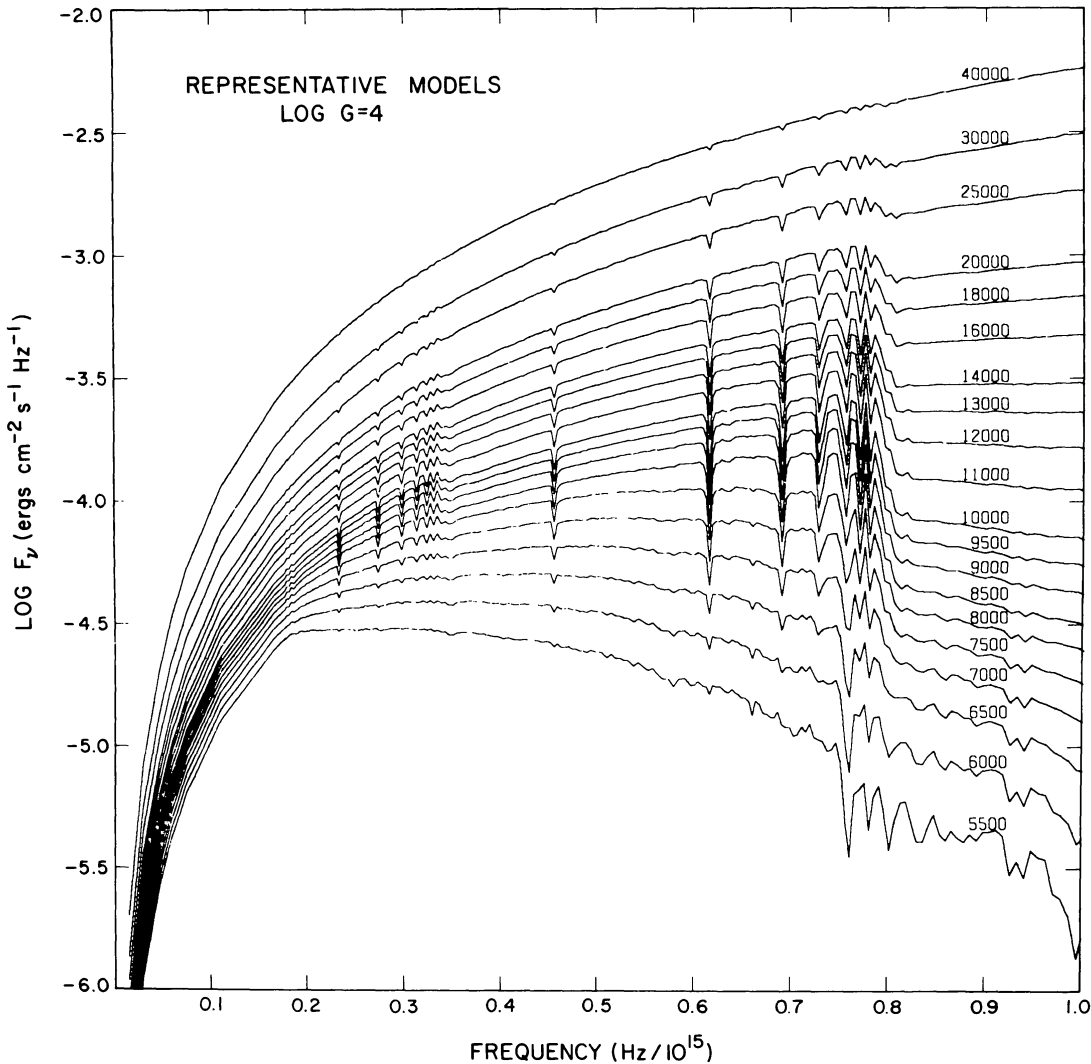


FIG. 15.—The flux F_ν visible from the ground as a function of T_{eff}

calibration. We will discuss the comparison of our models to this new calibration in § VI. We obtain an almost perfect match with a $T_{\text{eff}} = 9400$ K, $\log g = 3.95$ model.

Second, the artifact in the model fluxes at the Balmer discontinuity turned out to be a serious error. The hydrogen line opacity in that region arises from the 10 V second level. The Boltzman factor for that level and, consequently, the opacity, are strongly temperature dependent, but the distribution functions for line opacity had not been tabulated with resolution sufficient to treat such a strong temperature dependence. Furthermore, the wavelength resolution across the Balmer discontinuity was such that some computational error would have been introduced in U even if the opacity had been perfect.

Third, the calibration by Matthews and Sandage is seriously out of date. It does not internally reproduce the colors of Vega to 0.05 mag, although Vega was one of their calibrating stars. This is the main contribution

to the KPA error in $B - V$. Matthews and Sandage's method of calibration by computing colors from scanner observations is analogous to our method of computing colors from models (if we used more than one star) and ideally should be more reliable. Unfortunately, the scanner observations available to Matthews and Sandage were normalized to incorrect calibrations of Vega that introduced large errors in U . This constitutes the main contribution to the KPA error in $U - B$. Another problem with scanner observations is that they are usually not scans but discrete observations made at intervals to avoid strong lines, while continuous data are required for the integrations. Also, for Vega, the best observed star, the claimed errors (Hayes and Latham 1975) are large: 2% in the visible and 3% in the ultraviolet. Observations of other stars are known to vary by up to 3 times that value from one observer to another (Breger 1976).

On the basis of the experience of the errors cited above, we tabulated the distribution functions at

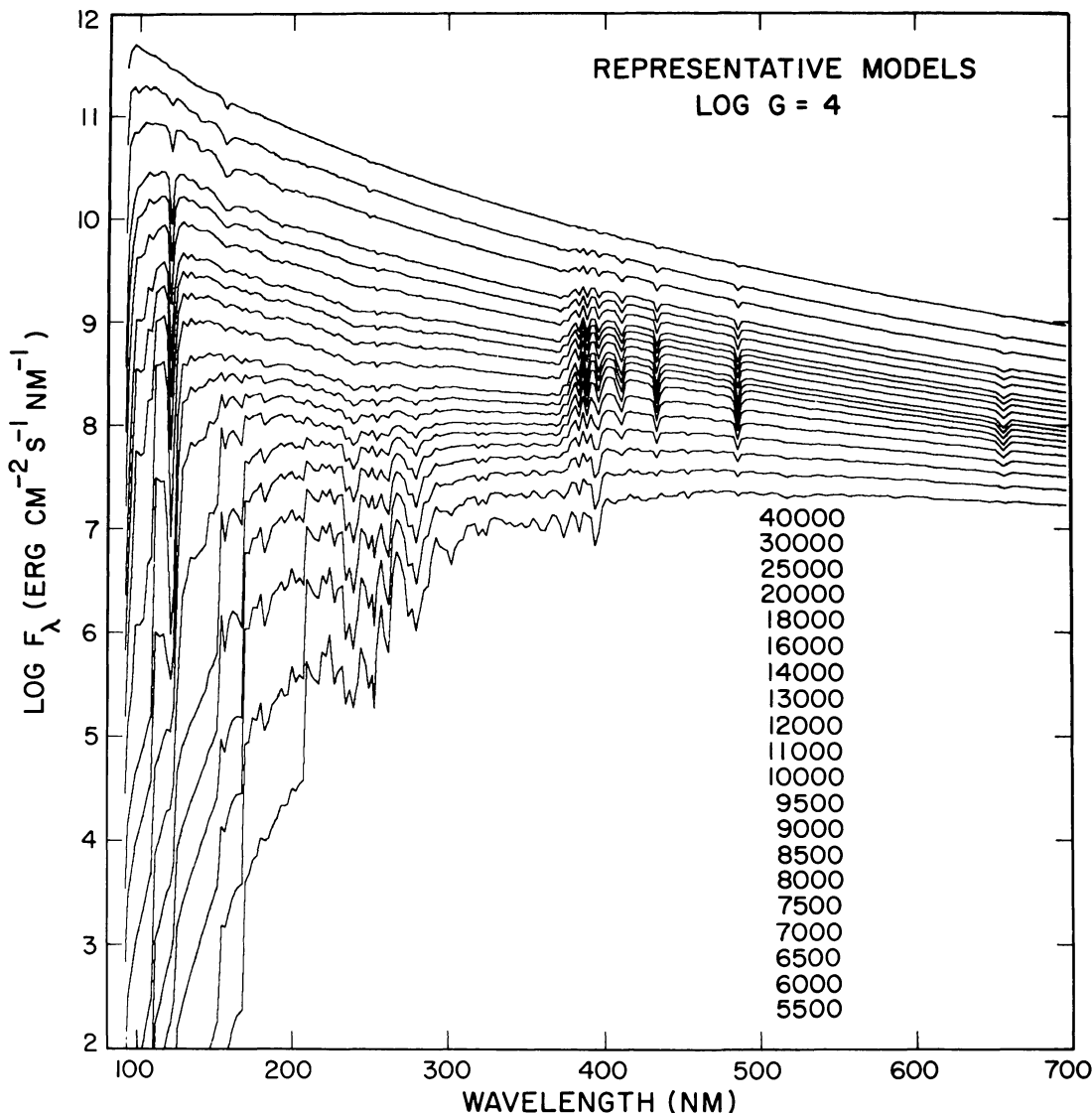


FIG. 16.—The flux F_λ redward of the Lyman limit as a function of T_{eff}

much closer spacing in $\log T$ to minimize interpolation errors in the opacity. We computed distribution functions and fluxes using much narrower bandpasses of 2.5 nm in U and B and 5.0 nm in V . Since we were able to compute a model that matches the Hayes and Latham calibration for Vega, we normalized our calculated colors to the observed colors for Vega. We expect the magnitude of systematic errors to be considerably reduced and the wavelength resolution to be adequate for us to compute $uvby$ as well as UBV colors.

There are seven systematic errors in this procedure, which, we hope, are small. (1) The calibration for Vega has errors. (2) The observed colors for Vega have errors and, in fact, have changed over the years (Blanco *et al.* 1970). (3) The theoretical photometric systems may be so unrealistic that they cannot be transformed to the “real” systems by simple constant

shifts. There may be color terms that can be determined only by comparing to many stars. The theoretical systems may be completely unphysical. (4) The numerical integration of the colors has errors. Ideally, the spectrum for each model should be calculated in detail. (5) There may be numerical problems remaining with the distribution functions or with the model atmosphere program itself. (6) The model parameters may be wrong; the microturbulent velocity or abundances may not be correct for the real stars. (7) The model physics may be wrong. The opacities might not be accurate, the convective treatment could be wrong, etc. Since we have not included molecular line opacity, we know that there must be some error in G stars. Relyea and Kurucz (1978) discuss the theoretical $uvby$ photometry in detail and compare to observations to test for such systematic errors. Other tests are described in § IV.

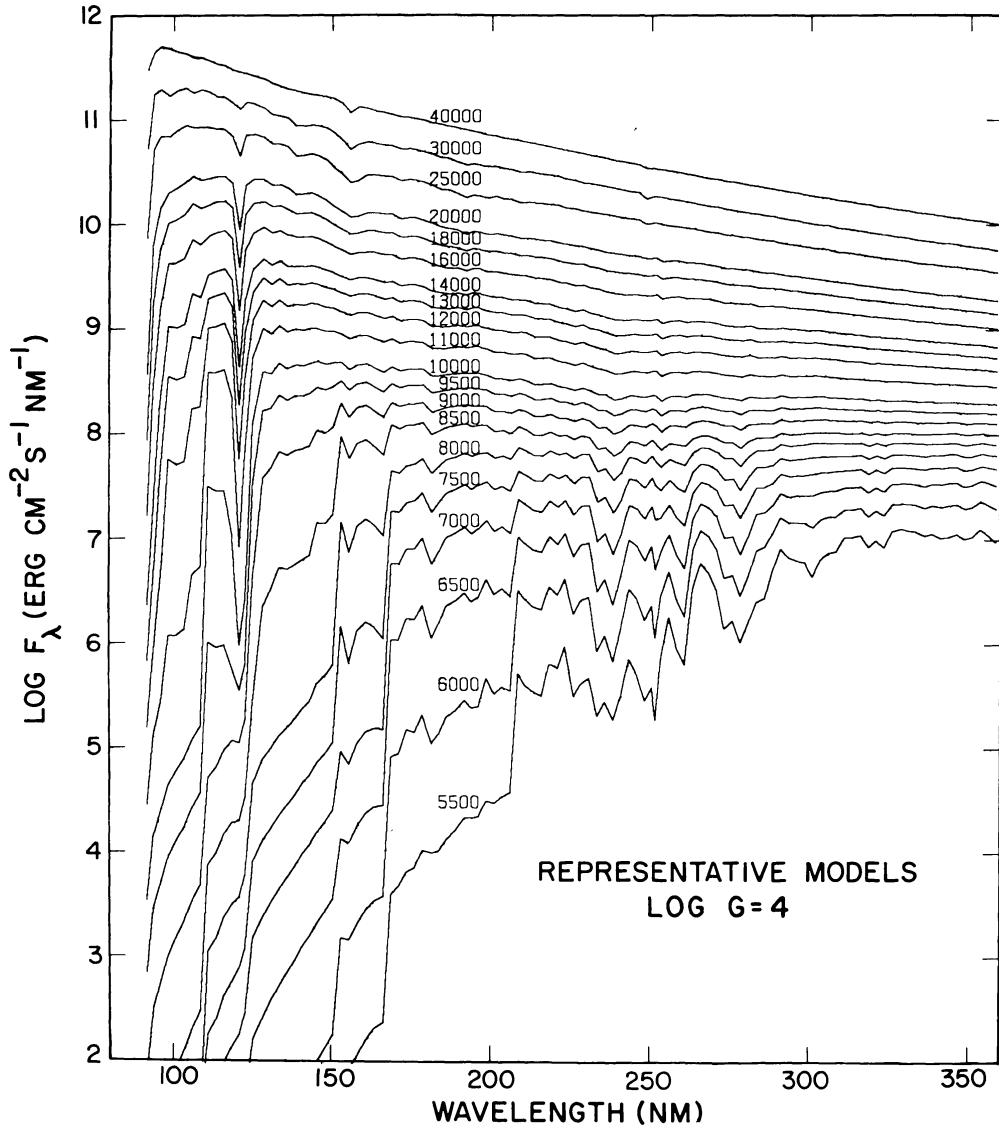


FIG. 17.—The ultraviolet flux F_λ observable from satellites as a function of T_{eff}

c) UBV

UBV colors are computed by following Matthews and Sandage, then normalizing to Vega. Since the U transmission function is defined at short wavelengths by the atmospheric cutoff, it is not defined for 0 air mass. Matthews and Sandage tabulated UBV transmission functions that include filters, a 1P21 photomultiplier, and two aluminum reflections at 1 and 2 air masses, which reduce the colors to 0 air mass. They also define B and V at 0 air mass. Their transformation equations, including their calibration, are

$$(B - V)_0 = 1.024(B - V)_1 + 0.91 \quad (26)$$

and

$$(U - B)_0 = 0.921(U - B)_1 - 1.308, \quad (27)$$

where the subscripts refer to the air mass. In practice, we compute the integrals

$$X = -2.5 \log \left[\int S_x(\lambda) F_\lambda d\lambda / \int S_x(\lambda) d\lambda \right], \quad (28)$$

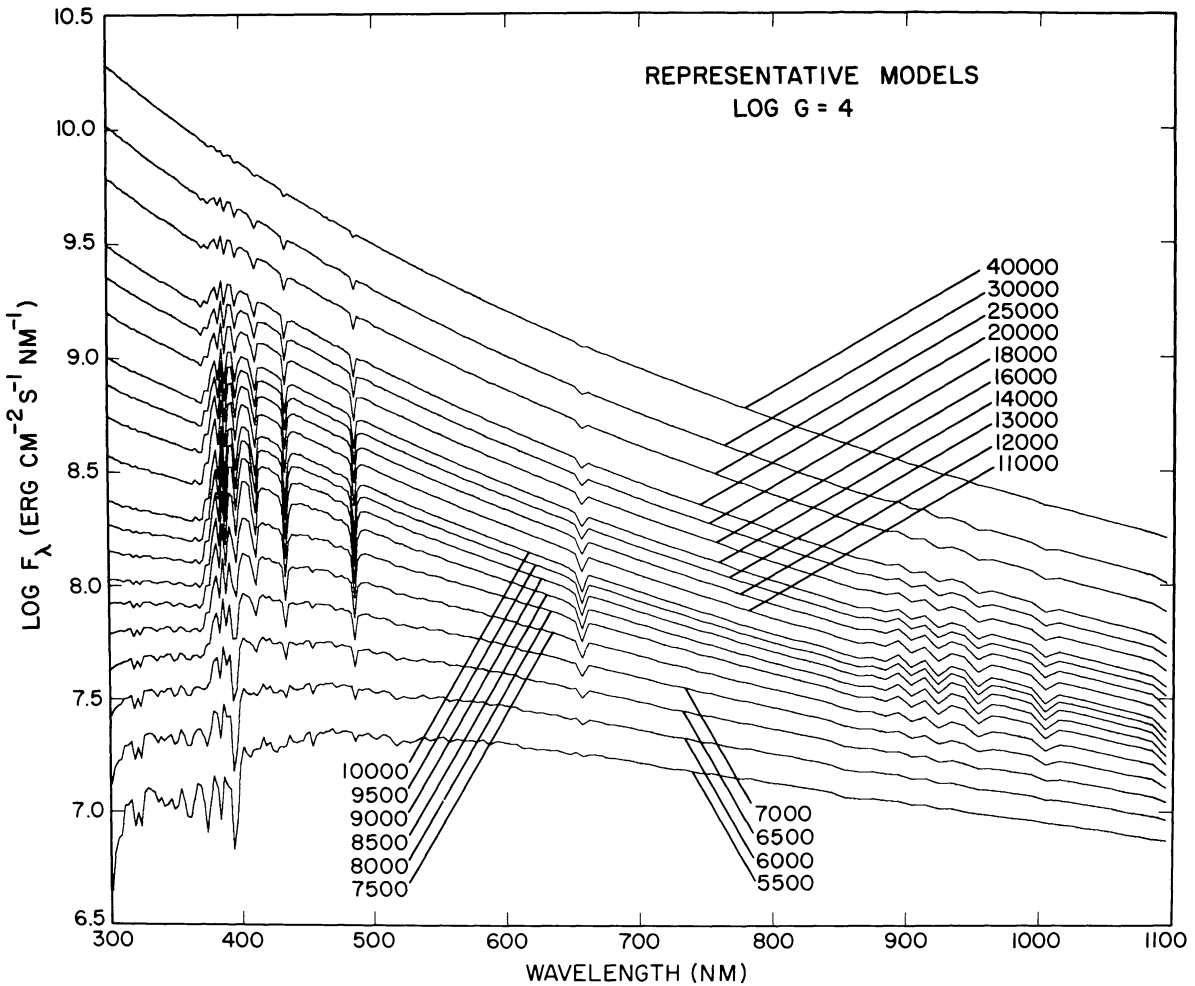
where $S_x(\lambda)$ is the transmission function for passband X , by interpolating $S_x(\lambda)$ parabolically and F_λ linearly to a wavelength spacing of 0.1 nm, then trapezoidally integrating. We compute U_1 , U_2 , B_0 , B_1 , V_0 , and V_1 and define

$$U_0 = 2U_1 - U_2, \quad (29)$$

$$(U - B)_1 = U_1 - B_1, \quad (30)$$

and

$$(B - V)_1 = B_1 - V_1. \quad (31)$$

FIG. 18.—The visible flux as a function of T_{eff}

U_0 , B_0 , and V_0 are the mean fluxes in the U , B , and V passbands, although U_0 is only approximate. To match the colors of Vega ($U - B = -0.01$ mag and $B - V = 0.00$ mag), we normalize

$$U - B = (U - B)_0 - 0.020 \quad (32)$$

and

$$B - V = (B - V)_0 + 0.022. \quad (33)$$

In Table 5A, U_0 , B_0 , V_0 , $U - B$, and $B - V$ are listed for each model.

Important note.—Relyea and Kurucz (1978) find systematic errors in our UBV colors. Buser (1978) has empirically modified the UBV filter transmissions using the work of Ažusienė and Stražys (1969) as a starting point. Buser and Kurucz (1978) have subsequently recomputed the UBV colors using the Buser filter transmissions instead of the Matthews and Sandage filter transmissions and find much better agreement with observations. In Table 5B we reproduce the improved colors from the Buser and Kurucz paper.

d) Bolometric Corrections

Only a fraction of a star's luminosity is visible through a V filter photometric system,

$$L_v/L = \frac{4\pi R_*^2 \pi \int C S_V(\lambda) F_\lambda d\lambda}{4\pi R_*^2 \pi \int F_\lambda d\lambda}, \quad (34)$$

where C is the absolute normalization of the V measurement system. If we define a bolometric magnitude as a measure of the stellar luminosity,

$$M_{\text{bol}} = -2.5 \log L + \text{constant}, \quad (35)$$

the difference between the bolometric magnitude and the V magnitude is the bolometric correction

$$\text{B.C.} = M_{\text{bol}} - V + \text{constant}. \quad (36)$$

By adjusting the constant, we define the smallest correction to be 0 and all other corrections to be negative, so that a bolometric magnitude is always

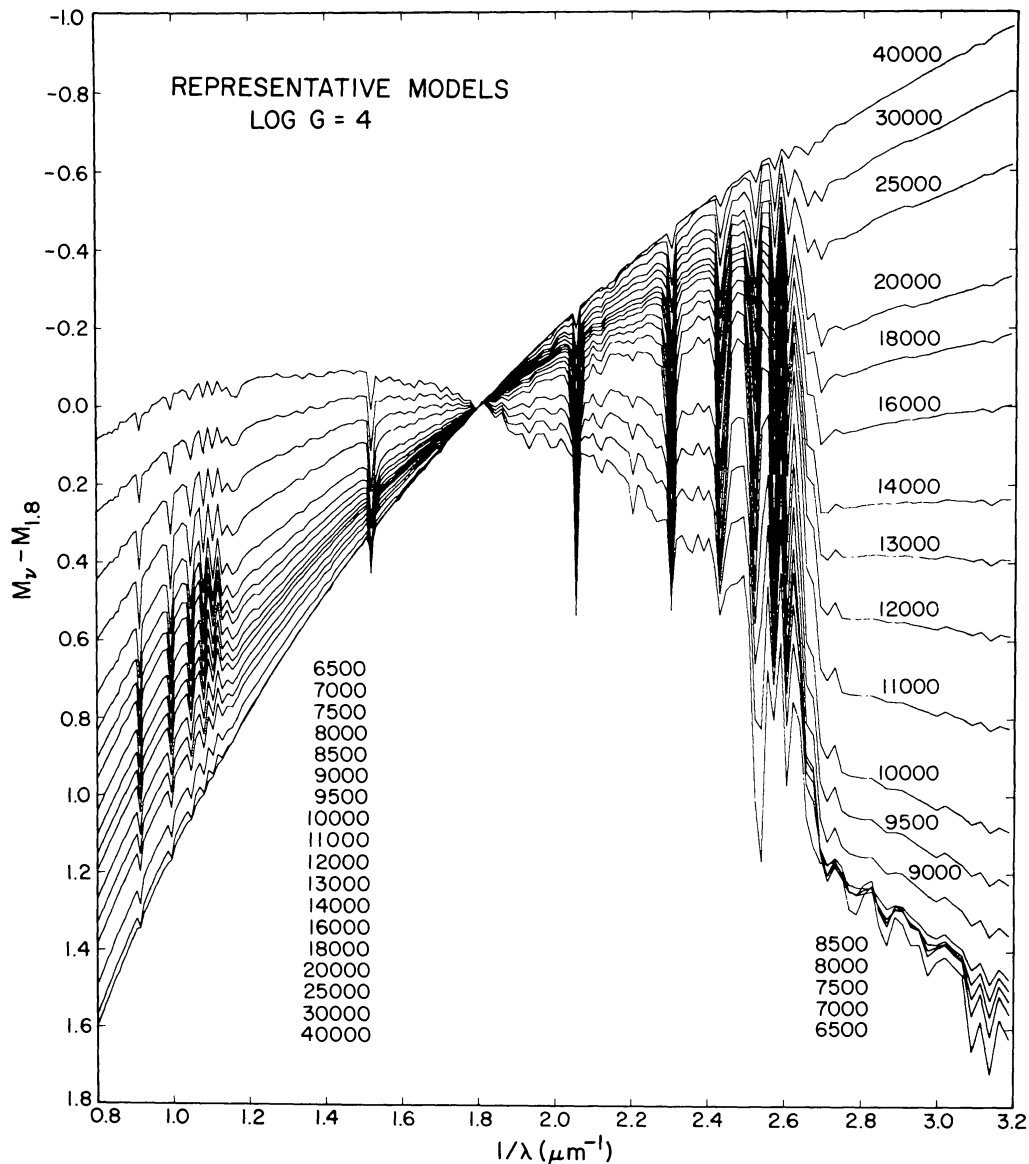


FIG. 19.—The visible colors, $M_v - M_{1.8}$, as a function of T_{eff} . This type of figure can be used to determine T_{eff} from spectrophotometry (cf. Fig. 26). Since $1.8 \mu\text{m}^{-1}$ is the approximate frequency of the V filter, approximate changes of $M_v - V$ with T_{eff} can be read off for any magnitude M_v .

brighter than a V magnitude. From equation (34) we see that

$$\begin{aligned} \text{B.C.} &= -2.5 \log F + 2.5 \log \int CS_V(\lambda)F_\lambda d\lambda \\ &\quad + \text{constant}, \end{aligned} \quad (37)$$

or, removing the coefficient C and normalizing the V magnitude,

$$\begin{aligned} \text{B.C.} &= -2.5 \log F \\ &\quad + 2.5 \log \left[\int S_V(\lambda)F_\lambda d\lambda / \int S_V(\lambda)d\lambda \right] \\ &\quad + \text{constant}'. \end{aligned} \quad (38)$$

We define

$$\text{B.C.} = \text{BOL} - V + \text{constant}', \quad (39)$$

where

$$\text{BOL} = -2.5 \log F = -2.5 \log (\sigma T_{\text{eff}}^4 / \pi). \quad (40)$$

BOL and V are listed in Table 5B for each model. The smallest value of $\text{BOL} - V$ is -6.986 at $T_{\text{eff}} = 7000 \text{ K}$, $\log g = 1$, so the bolometric correction is

$$\text{B.C.} = \text{BOL} - V + 6.986. \quad (41)$$

Other normalizations of the bolometric correction are possible, such as a constant for the bolometric correction of the Sun. As discussed in § VI, our model for

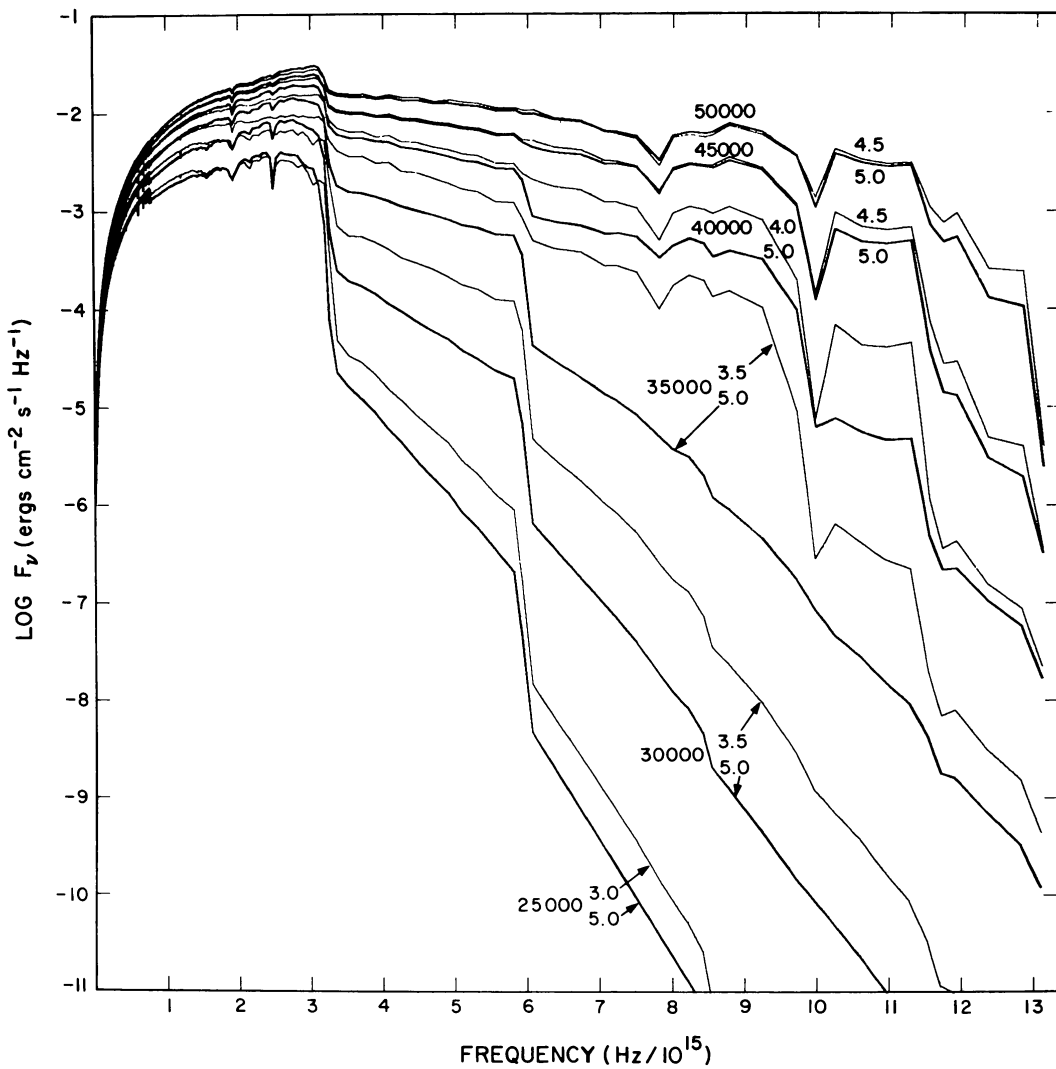


FIG. 20.—Flux F_ν for representative hotter models showing the Lyman and He I continua as a function of T_{eff} for the extremes of gravity calculated in this grid.

the Sun has approximately a 2% error in V , so the $T_{\text{eff}} = 5770$ K, $\log g = 4.44$ model cannot be used simply for defining such a bolometric correction. Further, the V magnitude for the Sun is not well known. To obtain a crude estimate, we can define

$$V_\odot = V_{5770} - 0.02, \quad (42)$$

$$\text{B.C.}_\odot = \text{B.C.}_{5770} + 0.02 = -0.194, \quad (43)$$

so that for a system where $\text{B.C.}'_\odot = -0.07$,

$$\text{B.C.}' = \text{B.C.} + 0.124. \quad (44)$$

A systematic error in the V magnitude for the $T_{\text{eff}} = 7000$ K, $\log g = 1$ model will, of course, introduce an error in the bolometric correction.

e) $uvby$

Intermediate-band $uvby$ colors were calculated including the effects of atmospheric transmission in a

manner similar to that of Matthews and Sandage. We used Matsushima's (1969) filter transmission curves, a standard 1P21 photomultiplier sensitivity curve obtained from Tapia (1974) and listed in Table 7, atmospheric transmission (Allen 1973), and the reflectivity of aluminum (Allen 1973). The wavelength dependence in the reflectivity of fresh aluminum is too small to affect the $uvby$ colors significantly. In real systems aluminum is dirty and has a time-dependent wavelength dependence that can affect u , but we are unable to treat such effects. We computed $uvby$ magnitudes for 0, 1, and 2 air masses. We also determined 0 air-mass magnitudes by reducing the 1 and 2 air-mass magnitudes to 0,

$$x_0' = 2x_1 - x_2, \quad (45)$$

analogous to the manner by which real observations are reduced. Atmospheric effects are negligible, except in u where the difference between u_0 and u_0' varies from 0.020 to 0.024 mag. We adopt u_0' as a better

TABLE 7
1P21 PHOTOMULTIPLIER SENSITIVITY

| λ | S | λ | S |
|-----------|------|-----------|------|
| 300 | 0.08 | 460 | 0.83 |
| 310 | 0.22 | 470 | 0.77 |
| 320 | 0.45 | 480 | 0.71 |
| 330 | 0.68 | 490 | 0.65 |
| 340 | 0.81 | 500 | 0.58 |
| 350 | 0.90 | 510 | 0.52 |
| 360 | 0.95 | 520 | 0.46 |
| 370 | 0.97 | 530 | 0.40 |
| 380 | 0.99 | 540 | 0.34 |
| 390 | 1.00 | 550 | 0.29 |
| 400 | 1.00 | 560 | 0.24 |
| 410 | 0.99 | 570 | 0.20 |
| 420 | 0.98 | 580 | 0.16 |
| 430 | 0.95 | 590 | 0.13 |
| 440 | 0.91 | 600 | 0.10 |
| 450 | 0.87 | | |

value than u_0 even though the variation of 0.004 mag is only marginally significant. In Table 5 we list u_0' , v_0 , b_0 , and y_0 , the mean fluxes in the filter passbands. The colors are computed from these magnitudes:

$$(u - b)_0 = u_0' - b_0, \quad (46)$$

$$(b - y)_0 = b_0 - y_0, \quad (47)$$

$$(m_1)_0 = (v_0 - b_0) - (b_0 - y_0), \quad (48)$$

$$(c_1)_0 = (u_0' - v_0) - (v_0 - b_0). \quad (49)$$

These colors were normalized to the observed colors of Vega (Crawford and Barnes 1970), $u - b = 1.411$, $b - y = 0.004$, $m_1 = 0.157$, and $c_1 = 1.089$, by using the normalizations

$$u - b = (u - b)_0 + 0.759, \quad (50)$$

$$b - y = (b - y)_0 + 0.479, \quad (51)$$

$$m_1 = (m_1)_0 - 0.055, \quad (52)$$

$$c_1 = (c_1)_0 - 0.090; \quad (53)$$

these colors are given in Table 5A.

As discussed in § VI, Relyea and Kurucz (1978) analyze *uvby* photometry using these calculated colors.

f) Balmer Line Profiles

Balmer line profiles computed with a program written by Peterson (1975) using the Vidal, Cooper, and Smith (1973) theory are presented in Table 8 (see pages 31 and 312). Figures 21–25 show examples of the variation with temperature and gravity that make the Balmer lines useful for determining gravities for early-type stars and temperatures for later types. We will discuss the comparison of these profiles to observations of Vega in § VI.

VI. COMPARISON TO OBSERVATIONS

The models presented here are reliable if they can predict the photospheric spectrum and energy distribution for stars that can be well observed. To test

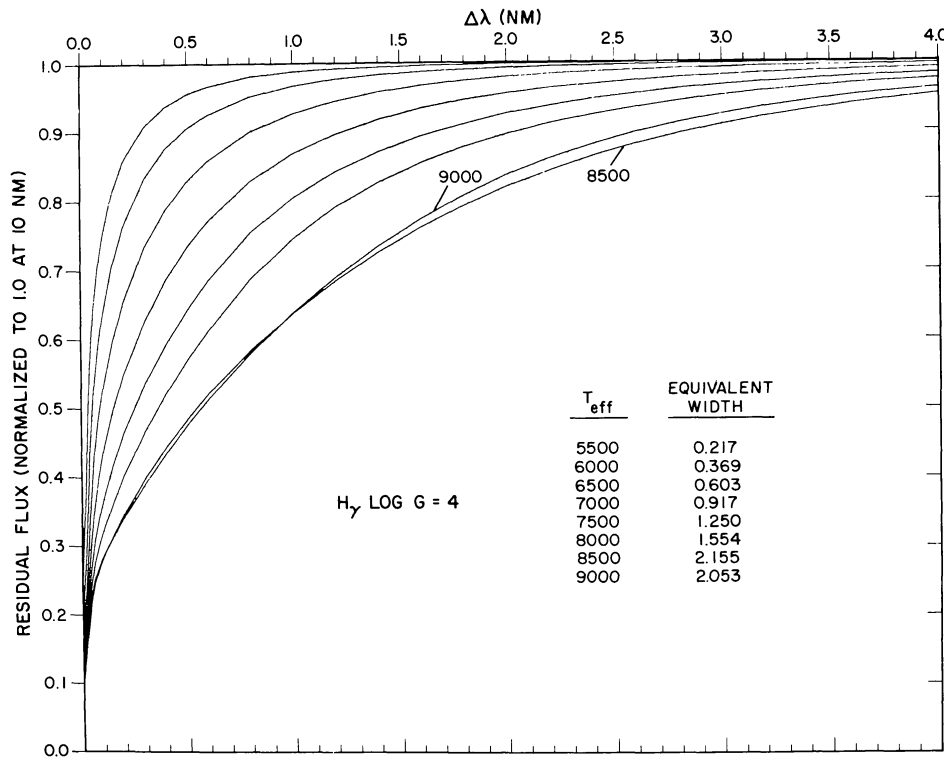


FIG. 21.— $H\gamma$ profiles for solar abundance models with $T_{\text{eff}} \leq 9000$ K. Equivalent widths are given in nm.

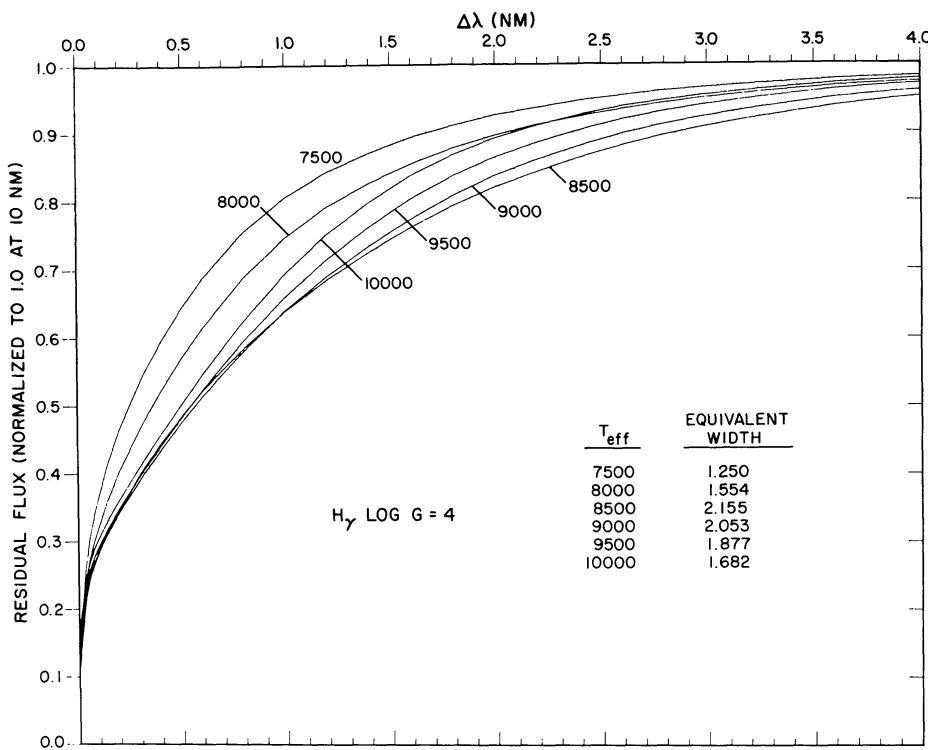


FIG. 22.— $H\gamma$ profiles for A star models showing the increase to maximum equivalent width

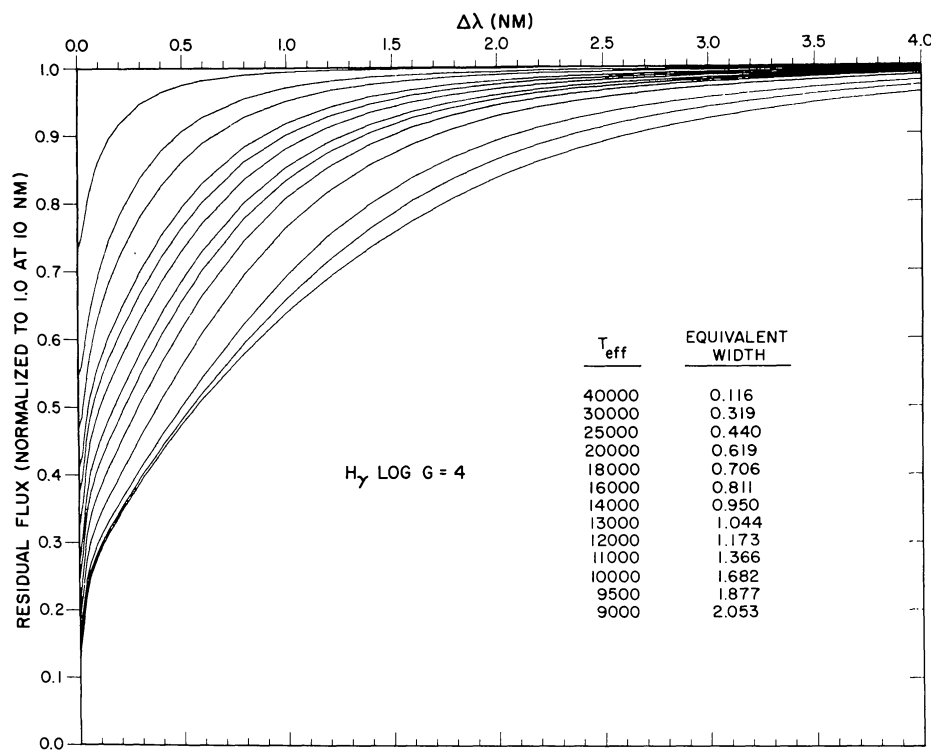


FIG. 23.— $H\gamma$ profiles for the early-type models showing the decrease in equivalent width with increasing T_{eff}

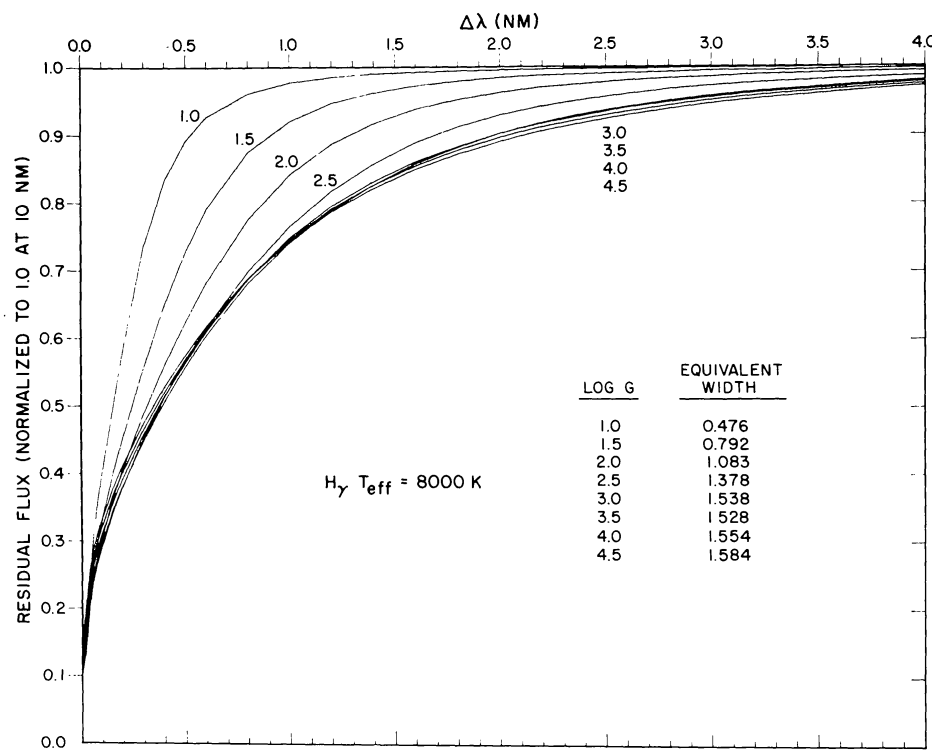
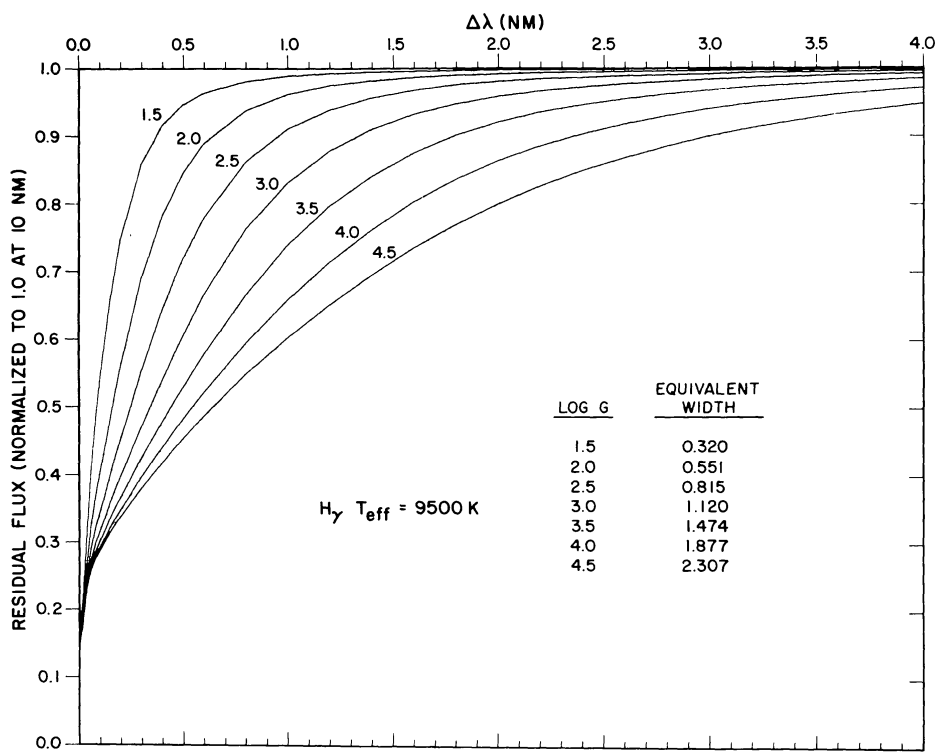
FIG. 24.— H_γ profiles as a function of gravity for $T_{\text{eff}} = 8000$ K— H_γ profiles as a function of gravity for $T_{\text{eff}} = 9500$ K, roughly A0, where the profile is ideal for gravity determination

FIG. 25.

the models and the completeness of our line opacity, we have projects under way for synthesizing the spectra of bright stars, starting with the Sun and Vega. That work is proceeding slowly because of difficulties in obtaining the high-resolution spectral atlases and because of the large amount of computer time required.

At lower resolution we can compare Balmer line profiles and energy distributions. We will discuss those comparisons in this section.

At still lower resolution we can compare to colors, as discussed in a paper by Relyea and Kurucz (1978) on the theoretical analysis of *uvby* photometry. They find excellent agreement between theoretical *uvby* colors predicted from these models and the observations for effective temperatures above 8000 K. For the late A and F stars there is a small systematic error in the colors that may be caused by an inadequate treatment of convection (these stars are weakly convective) or some other reason. Detailed spectral comparisons for models with various treatments of convection, microturbulence, etc., will be required in order to resolve the problem. The colors for the G star models are slightly affected by the lack of molecules in our calculation. The errors do not seem to affect greatly the use of the *uvby* colors differentially.

Relyea and Kurucz find that *UBV* colors (Table 5A) are systematically in error because the *U* filter cannot be adequately defined theoretically. Empirical corrections must be made to the theoretical colors if they are to be used. Relyea and Kurucz did not investigate further because the *uvby* colors are much more useful for testing the models and for determining stellar parameters.

Buser and Kurucz (1978) have subsequently recomputed the *UBV* colors (Table 5B) using empirically modified filter transmissions (Buser 1978). They find the same effects for *UBV* that Relyea and Kurucz found for *uvby*, agreement with observation for effective temperatures above 8000 K, and a small systematic error for cooler stars.

We now turn to the intermediate-resolution comparisons. Vega is the star with the best known energy distribution and is used as the fundamental spectrophotometric standard. The recent revised calibration of its colors by Hayes and Latham (1975), shown in Figure 26, claims accuracies of 2% in the visible and infrared and 3% in the ultraviolet. Balmer line profiles, shown in Figure 27, have been observed by Peterson (1969), who claims an accuracy of $1\frac{1}{2}\%$. We have computer programs that plot the colors of any model in the grid together with observed colors (cf. Figs. 19 and 26), and a similar program for Balmer line profiles (cf. Figs. 25 and 27). From the colors we determine the theoretical parameters $T_{\text{eff}} = 9400 \pm 200$ K and $\log g = 4.0 \pm 0.5$. Then from the Balmer lines we find $\log g = 3.95 \pm 0.05$. A model was computed with these parameters and is included in this grid. Figure 26 shows the remarkably good fit to the colors. We note that the slopes of the Brackett, Paschen, and Balmer continua are consistent with the observations as are the colors relative to $1.8 \mu\text{m}^{-1}$, except perhaps between the Balmer lines. Figure 27 shows the excellent Balmer line fit for $H\alpha$, $H\beta$, and $H\gamma$. There is a small discrepancy in that the Balmer line cores are narrower than those observed. However, Vega has a projected rotational velocity of approximately 25 km s^{-1} . Rotationally broadening the theoretical profile would widen

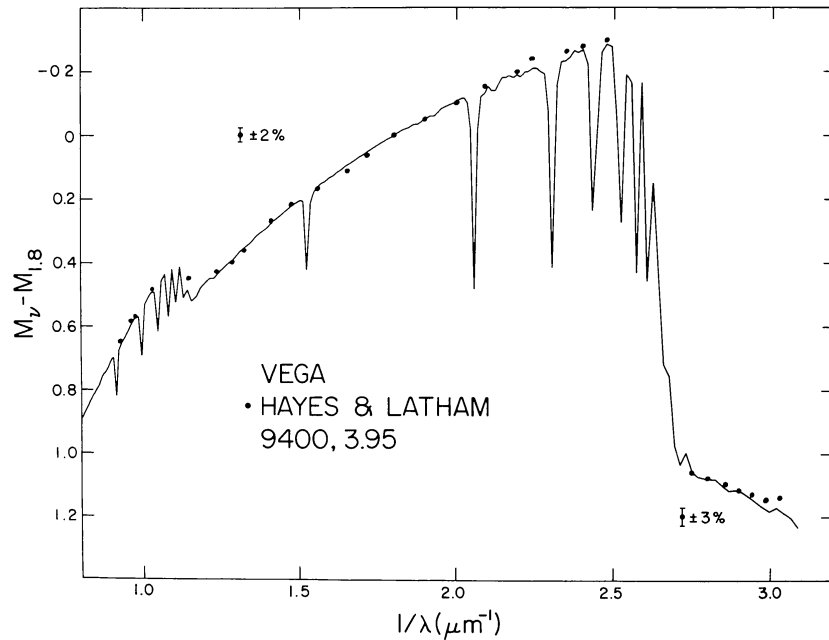


FIG. 26.—Comparison of the colors of the 9400, 3.95 model with the recalibration of Vega by Hayes and Latham (1975). Error bars for the observations are indicated.

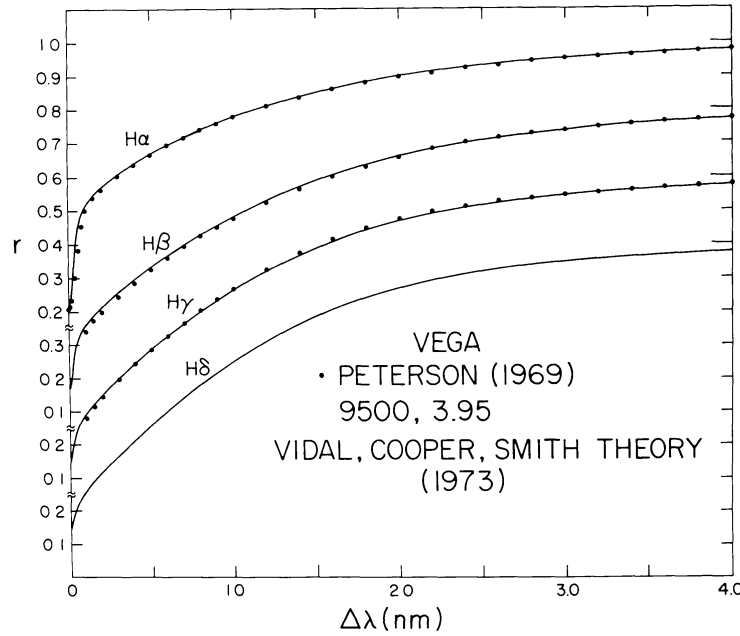


FIG. 27.—Balmer line profiles for the model shown in Fig. 26 compared to the observations of Peterson (1969)

the core to match the observations without noticeably affecting the wings. The central residual intensity would then be too high, but non-LTE effects, which have not been included, would lower the central depth of the lines (Peterson 1969). Thus we conclude that our model calculation is in excellent agreement with the intermediate-resolution observations of Vega.

Tüg, White, and Lockwood (1977) have remeasured the energy distribution of Vega, and their colors agree with those of Hayes and Latham. Figure 28 shows the excellent agreement of our Vega model with their

observations. The difference at the Paschen limit arises because their narrow bandpass resolves higher-series lines.

Our effective temperature of 9400 K is consistent with an earlier value of 9650 K found by Schild, Peterson, and Oke (1971) using models that included only hydrogen lines. Since the new models have more opacity, they should produce approximately the same colors at a lower effective temperature. Our parameters are also consistent with the empirical values determined by Code *et al.* (1976) and Code (1975) of

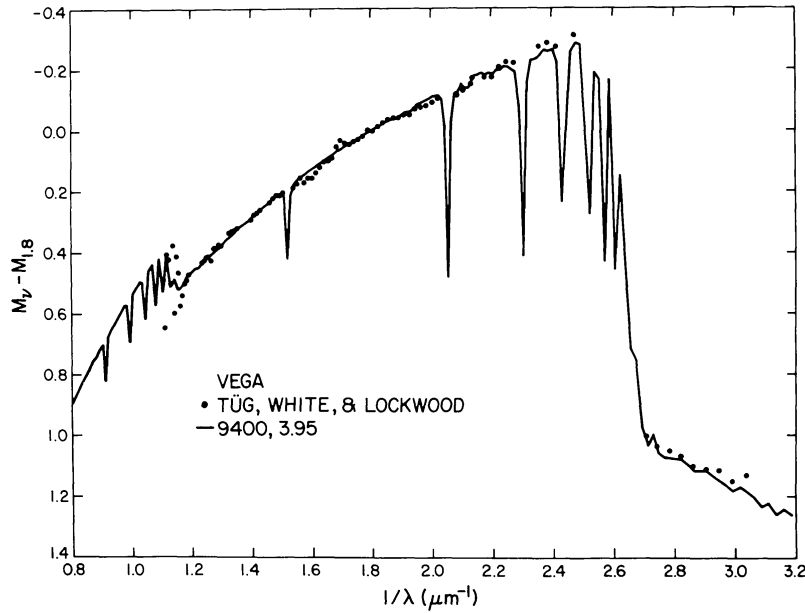


FIG. 28.—Comparison of the colors of the 9400, 3.95 model with the calibration of Vega by Tüg, White, and Lockwood (1977)

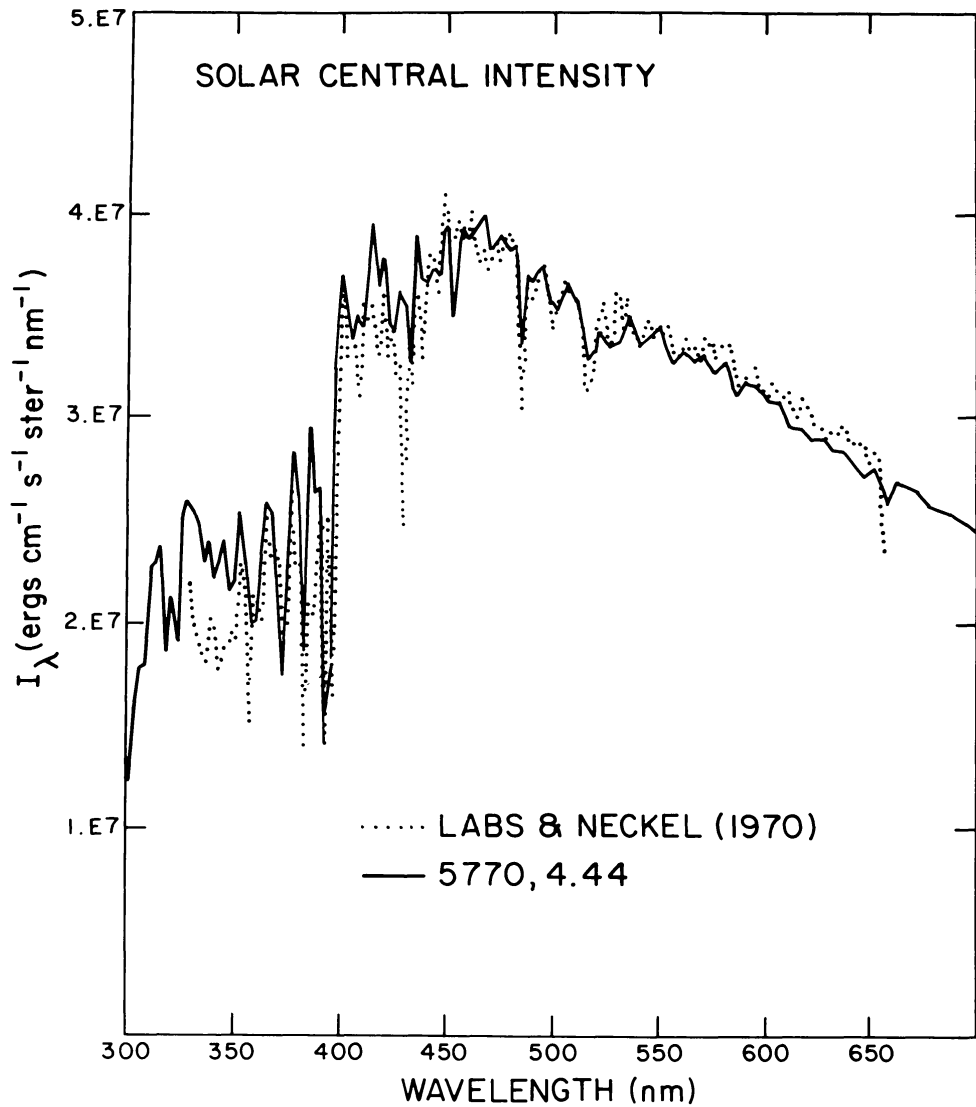


FIG. 29.—Solar central intensity computed from the 5770, 4.44 model compared to the observations of Labs and Neckel (1970)

9660 ± 140 K and 3.94 ± 0.08 , respectively, in the sense that the error limits overlap.

Observations to similar accuracy have also been made by Labs and Neckel (1968, 1970) for the solar central intensity. We computed a model with $T_{\text{eff}} = 5770$ K, $\log g = 4.44$ and predicted the central intensity for comparison to their observations as shown in Figure 29. Since molecular lines are not included, the G band at 430 nm is too weak and the calculated intensity at 340 nm is too high. In our opinion, the low intensity in the red is consistent with not enough opacity in the model from molecules. As discussed in § I, this comparison indicates just the small discrepancies that we would expect from our limited line data.

Lower-accuracy rocket and satellite observations of Vega and the Sun are also available. In Figure 30 we show the flux at the Earth observed by the *AOO 2*

satellite (Code and Meade 1976) and by the *TD 1* satellite (Jamar *et al.* 1976) together with our model for Vega normalized at 310 nm. The correspondence is generally good in the features above 190 nm. The dip at 240 nm is caused by Fe II resonance lines that may be too strong. The overall level seems to be slightly less than the *TD 1* measurements. If those measurements are correct, the model must be very close to correct. If the *AOO 2* measurements are correct, the model has a significant overestimate of the line opacity between 130 and 200 nm that would result in a slight underestimate of the effective temperature.

In Figure 31 we show a solar rocket flux measurement by Broadfoot (1972) plotted with our predicted solar flux at the solar surface. The model is generally higher in the ultraviolet as expected because molecular opacity is not included. The computations of Fe II lines around 240 nm are too strong, which probably results

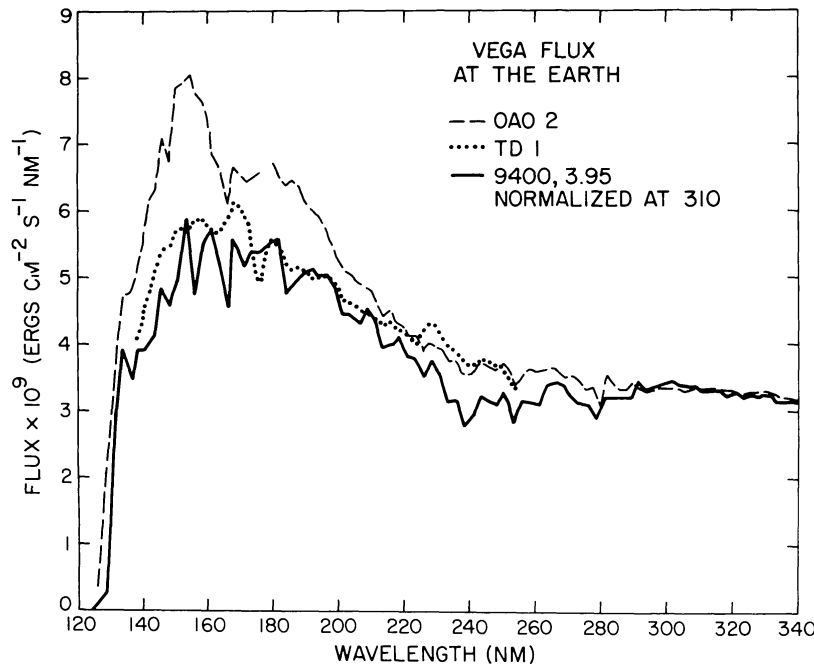


FIG. 30.—Observed ultraviolet flux from Vega at the top of the atmosphere compared with our model for Vega. The *OAO 2* measurements are from Code and Meade (1976). The *TD I* measurements are from Jamar *et al.* (1976).

from overestimated damping constants. As mentioned above, we are making detailed spectral comparisons to investigate the discrepancies.

Comparisons should be made between our predicted fluxes and all the normal stars in the *OAO 2*, *TD I*, and Breger (1976) spectrophotometric catalogs, but we have not yet done so.

VII. COMPARISON WITH OTHER GRIDS OF MODELS

In this section we compare our results with other large-scale grids of models that have attempted to include all the line opacity and that overlap our temperature range. These include the grids of Carbon and Gingerich (1969); Peytremann (1970, 1974a, b);

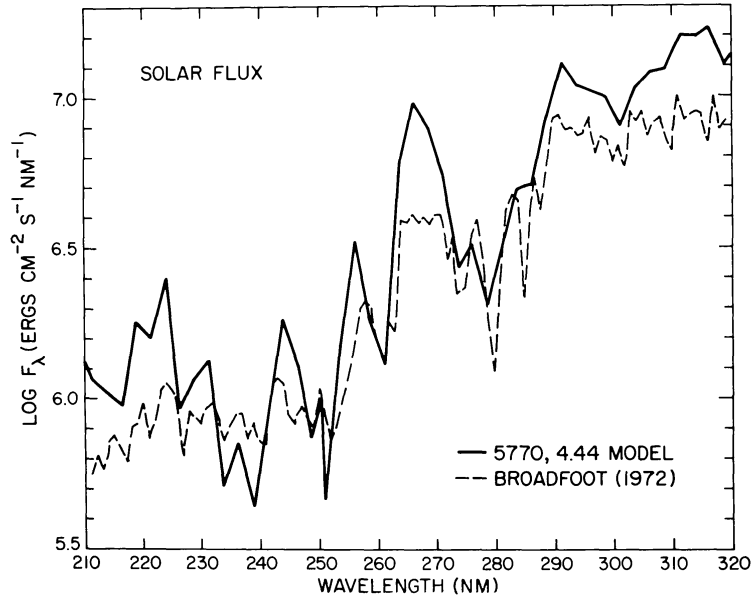


FIG. 31.—Flux F_ν for our solar model compared to the ultraviolet flux observations by Broadfoot (1972). Broadfoot tabulates N_λ (photons $s^{-1} cm^{-2} \text{\AA}^{-1}$), and the conversion is F_ν (ergs $cm^{-2} s^{-1} nm^{-1}$) = $10^{12} N_\lambda h\nu (d/R_\odot)^2 / \pi = 2.9210 \times 10^8 N_\lambda / \lambda$ for λ in \AA and $d = 1 \text{ AU}$.

Gustafsson *et al.* (1975) and Bell *et al.* (1976, both hereafter GBEN); and KPA. We also compare our results with the widely referenced LTE and non-LTE models of Mihalas (1972), which give an indication of our error in assuming LTE.

The Carbon and Gingerich grid was an early attempt to use a distribution-function representation for the line opacity. They did not have atomic data sufficient to compute the distribution functions but, instead, produced empirical three-step distribution functions by varying the parameters to force a match to the observed visible blocking of a few bright stars. They guessed the ultraviolet opacity. The models labeled "old" in Figures 1, 2, and 3 are Carbon and Gingerich models, while those labeled "new" are ours. Their procedure clearly underestimated the opacity for the earlier-type stars and produced models with too shallow a temperature gradient.

Peytremann computed a grid of models in which he used a sampling technique to evaluate integrals over the radiation field. He chose 600 frequencies and evaluated the line opacity explicitly at each one. However, the line data that were available to him were the same as those used by Strom and Kurucz (1966) in the first attempt at a distribution-function model and were considerably deficient. He therefore introduced pseudolines, similar to the lines he already had, sufficient to produce a reasonable solar model. In Figure 32 we show Peytremann's 8500, 2, -1 model (where we use the notation T_{eff} , $\log g$, \log abundance relative to solar to identify a model), which is the

hottest model in his grid. The agreement is very close, generally within 100 K. If we ignore the surface drop, the higher temperature in our model indicates slightly more opacity. We hypothesize that the lower surface temperature in the Peytremann model is caused by having too much opacity in line cores that become optically thin at $\log \tau_{500} = -2.5$. This could arise because his pseudolines were given the same properties as the lines for which data existed, but those lines are the stronger lines through selection effects. In fact, the missing lines would tend to be weaker and not contribute so much "core" opacity. Alternatively, his frequencies might accidentally fall on too many line cores. Figure 33 shows the comparison of our solar models, but the comparison is complicated by the increased convection in our model. Our interpretation is that in this model also we have slightly more opacity.

KPA computed a grid of models for early-type solar abundance stars covering the range from 8000 to 50,000 K using essentially the same data and technique that we use here. The difference is that we have used higher resolution in temperature and wavelength in tabulating the distribution functions because their tabulation was so coarse that it introduced serious interpolation errors in the opacity. This led to an underestimate of the opacity and to models with too shallow a temperature gradient as shown in Figures 34, 35, and 36. Thus effective temperatures derived from the KPA energy distributions should be systematically slightly high.

By use of the KPA distribution functions Kurucz (1974) also computed a solar model that is shown in

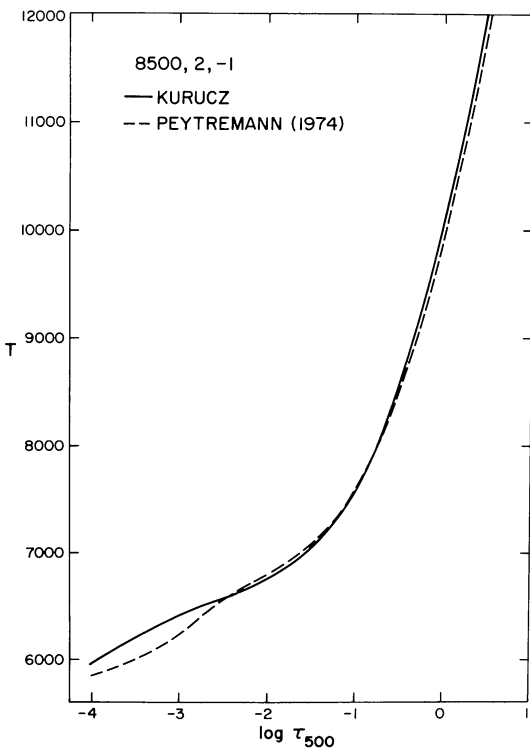


FIG. 32.—Comparison of our 8500, 2, -1 model $T - T_{500}$ relation with that of Peytremann (1972).

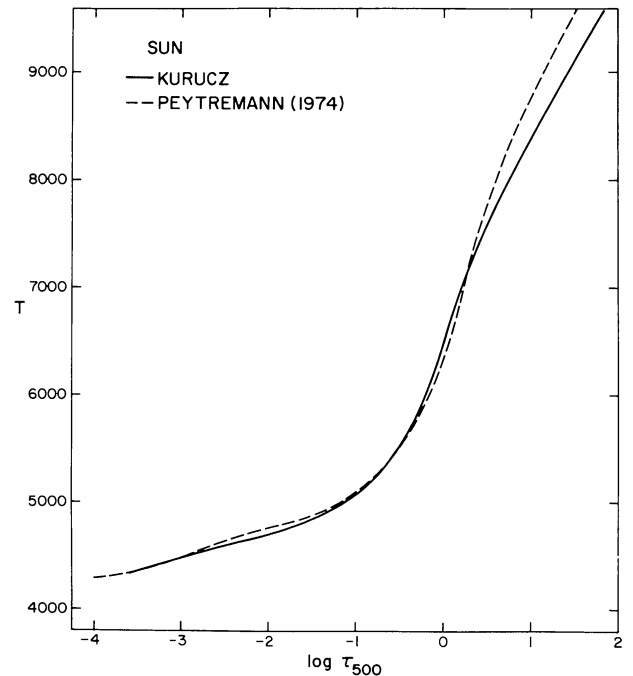


FIG. 33.—Comparison of our solar model with that of Peytremann (1974a, b).

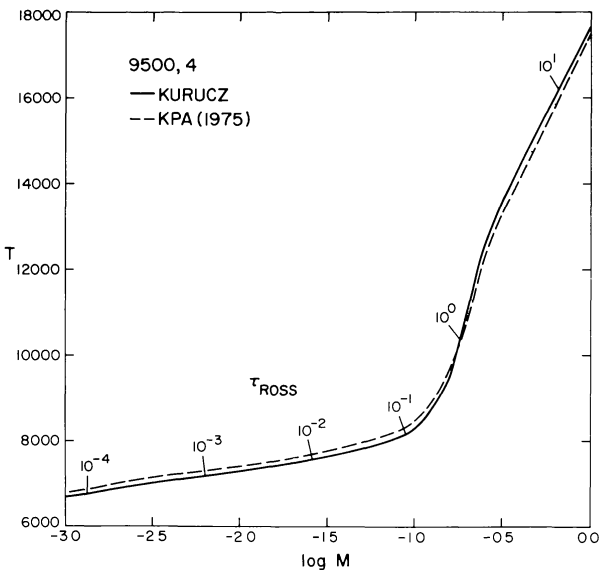


FIG. 34.—Comparison of our 9500, 4 model with that of KPA. Rosseland optical depths are indicated.

Figure 37. The opacity errors produce small temperature differences from our present model, but these are much smaller than the differences from other theoretical models that arise from different treatments of convection and opacity.

We also compare our model with two widely referenced empirical models: the HSRA model by Gingerich *et al.* (1971) and the model by Vernazza, Avrett, and Loeser (1976, hereafter VAL), which are shown in Figure 38. It is likely that mechanical heating, which is not included in our radiative equilibrium

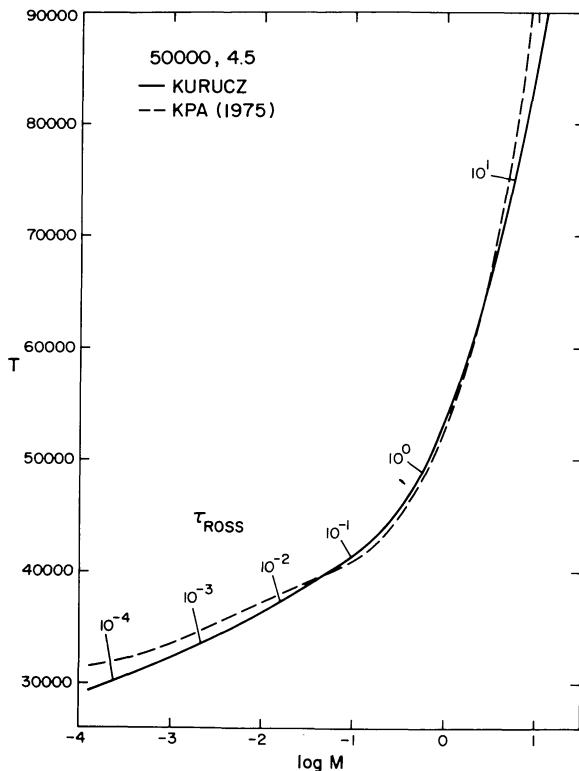


FIG. 36.—Same as Fig. 34 for 50,000, 4.5

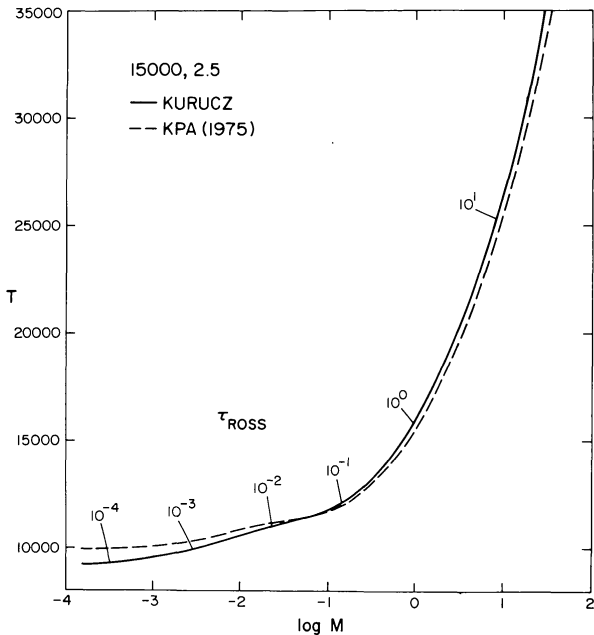


FIG. 35.—Same as Fig. 34 for 15,000, 2.5

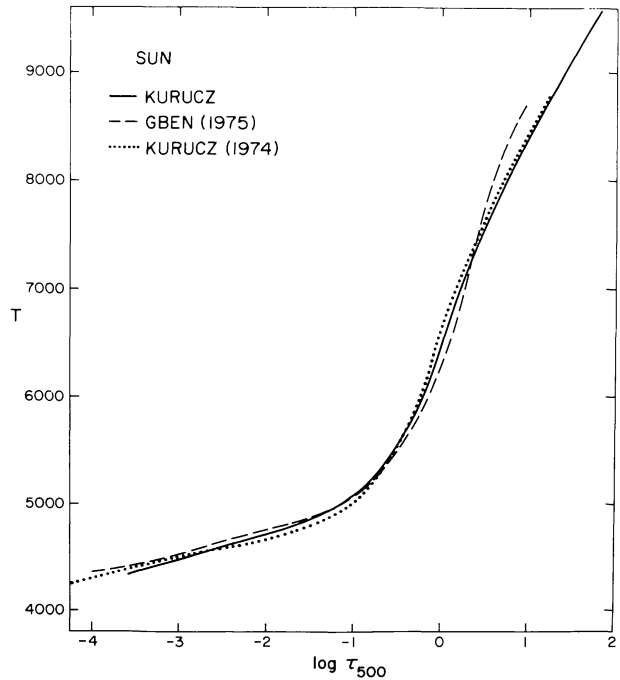


FIG. 37.—Comparison of our solar model with the models of Kurucz (1974) and GBEN.

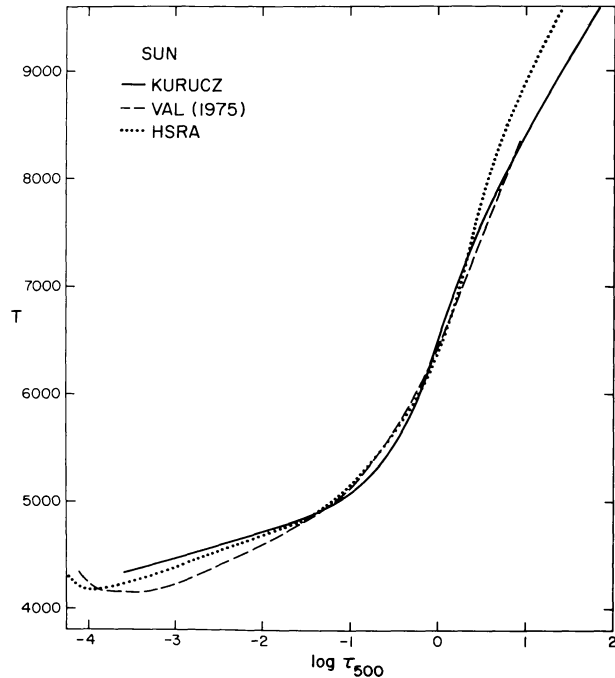


FIG. 38.—Comparison of our solar model with the VAL and HSRA empirical models.

model, would raise the temperature at the temperature minimum as well as in the chromosphere. Thus we expect a realistic radiative equilibrium model to have temperatures in the temperature-minimum region lower than those in a realistic empirical model that necessarily includes the heating. However, our model lies above these empirical models in the temperature-minimum region. As discussed in § V, our solar model has insufficient opacity because it does not include molecules. Thus its temperature gradient is too shallow and its temperature in the temperature-minimum region is too high. Thus part of the discrepancy lies in our model, but it is also possible that these empirical models are incorrect and should be, say, 200 K hotter in the temperature-minimum region.

The GBEN models for later-type stars were computed with a statistical distribution-function representation of the line opacity that is similar to ours. Their line data were determined by empirically fitting the solar spectrum in the visible and from laboratory data, and include both atomic and molecular lines. However, their ultraviolet line data are incomplete. Also, they assume narrower lines, a 2 km s^{-1} total Doppler width, instead of our 2 km s^{-1} microturbulent velocity. When we compare solar abundance models (Figs. 37 and 39), no great difference is apparent, except in the convection zone, $\tau_{500} > 2$, where the difference is due to our various treatments of convection. The agreement at shallow layers indicates that the models have approximately the same total opacity. Our increased ultraviolet atomic opacity and Doppler width apparently balance GBEN's molecular opacity and narrower Doppler width. In Figure 40 we

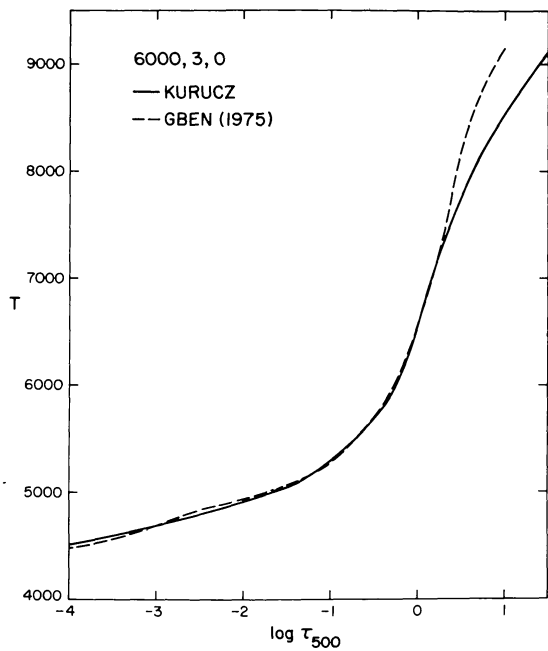


FIG. 39.—Similar to Fig. 37 for 6000, 3.0

show models for a Population II G giant. In this case our model clearly has more opacity. Improved model calculations and detailed spectrum comparisons will be made to explain the difference.

Mihalas has published grids of models for O and B stars including both LTE and non-LTE calculations. The models do not include metal line opacity. A comparison with two examples that show large differences between LTE and non-LTE models is shown in Figures 41 and 42. The differences between

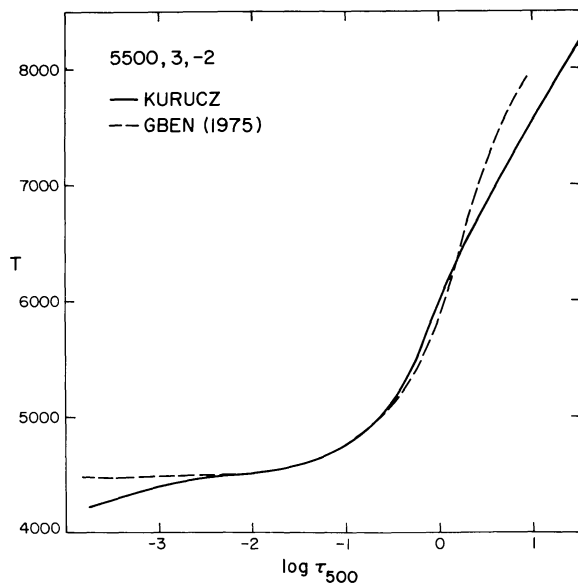


FIG. 40.—Similar to Fig. 37 for 5500, 3, -2

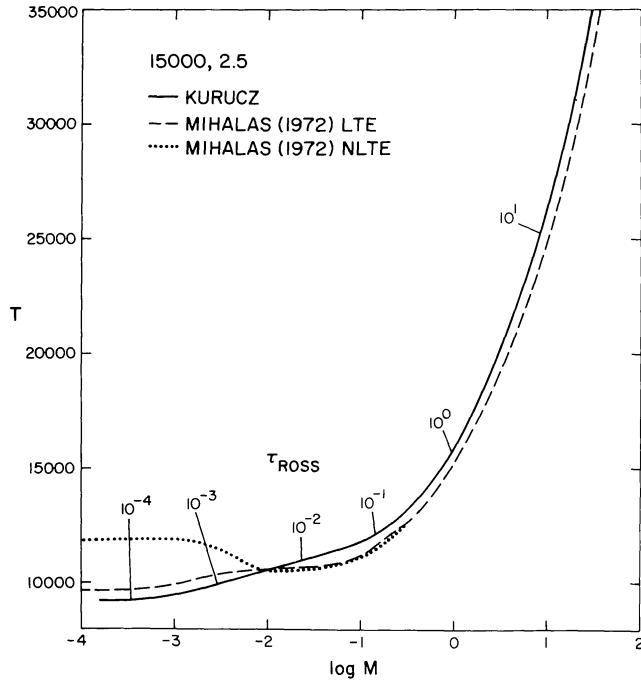


FIG. 41.—Comparison of our 15,000, 2.5 model to LTE and non-LTE models by Mihalas (1972).

the Mihalas LTE and non-LTE models show the magnitude of the errors that might be expected in our hottest and lowest-gravity models because of the LTE approximation. Such errors decrease rapidly as the gravity increases. The reader should note the significant errors in the Mihalas LTE models compared to our model, for $\tau_{Ross} > 10^{-2}$, because sufficient line opacity was not included. Thus neither grid of models is accurate, but ours is more reliable at higher gravities for predicting continua and weak lines. A non-LTE calculation that treats all the lines is currently beyond the state of the art, but an approximation where hydrogen and helium are treated in non-LTE with other lines in LTE might be feasible.

These models were computed in 1974, 1975, and 1976 at Kitt Peak National Observatory, the State University of New York at Albany, and the Smithsonian Astrophysical Observatory using the equivalent of 400 hours of CDC 6400 computer time. We are especially grateful to Dr. Lawrence Relyea for providing time at Albany and for the considerable assistance and encouragement he gave to this project. We thank the computer staff at Kitt Peak National Observatory for their help and patience. We thank Dr. Bruce Carney for critical comments on the text.

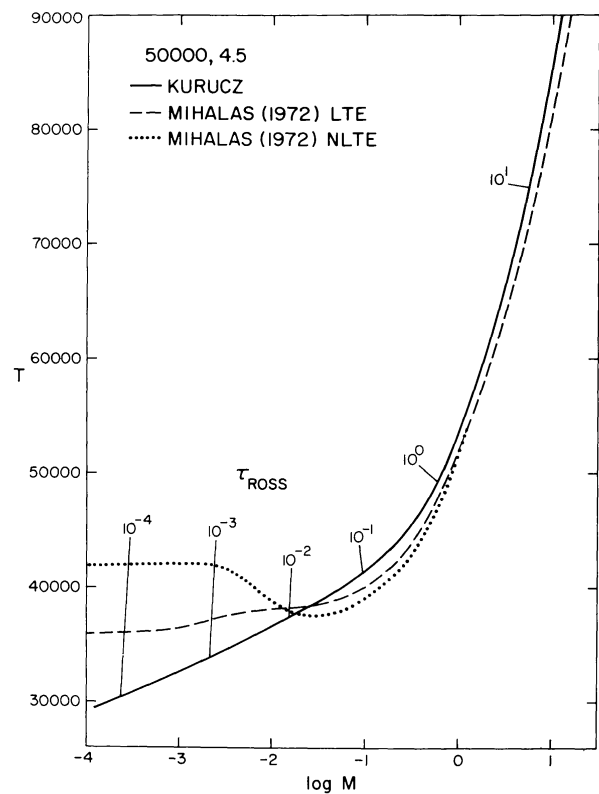


FIG. 42.—Same as Fig. 41 for 50,000, 4.5

Note added in manuscript, 1978 November.—As of this writing, we have available the following additional material:

Tapes of distribution functions for 10, 3, 1/3, 1/30, 1/300, 1/1000, and 0 times solar abundances. We plan to compute grids of models for these abundances as computer time becomes available.

Limb darkening for all the models listed here. With Dr. Brian Flannery we plan to investigate rotation and binary light curves. We are open to collaboration.

Predicted infrared fluxes for Vega and Sirius.

A and B star models for 10 and 3 times solar abundance.

Distribution functions leaving out hydrogen lines. We plan to use these together with accurate H β profiles to produce H β indices.

Thirteen-color photometry for all the models listed here.

Note added in proof, 1979 March.—We have now computed grids of model atmospheres for 10, 3, 1, 1/3, 1/10, 1/30, 1/100, 1/300, 1/1000, and 0 times solar abundances for the temperature range 5500–8500 K. We also have models for A and B stars for 1/3 and 1/10 times solar abundances.

NOTES TO TABLES 4, 5, 6, AND 8

TABLE 4.—There are 140 solar abundance models, 72 1/10 solar abundance models, and 72 1/100 solar abundance models listed two per page. The heading for each model gives the effective temperature, log surface gravity, log metal abundance relative to solar, and whether the model is convective plus radiative or purely radiative. The 40 depths actually used in the computation are listed, roughly equally spaced in $\log \tau_{\text{Ross}}$ from -4.5 to 2.0 in steps of $\frac{1}{6}$. Owing to scaling from model to model and to radical temperature corrections, this spacing is not always maintained. To compress the tables, all the variables except temperature are given as logs. The units are cgs for all variables. The columns are mass per unit area, Rosseland optical depth, continuum optical depth at 500 nm, geometric height, temperature, pressure, electron number density, atom number density, mass density, Rosseland mass absorption coefficient, continuum mass absorption coefficient at 500 nm, radiation pressure, radiative acceleration, and the fraction of flux carried by convection. The first values of τ_{Ross} , τ_{500} , and x are defined to be 0. Depths with no convection are listed with 0 convection fraction.

TABLE 5.—Predicted colors in the *UBV* and *uvby* systems as described in § Vb are listed for each model. The columns are effective temperature; log surface gravity; log metal abundance relative to solar; mean magnitudes in the *U*, *B*, and *V* passbands, which are equal to -2.5 times the log mean flux F_{λ} ; the bolometric magnitude, which is -2.5 times the log integrated flux F ; $U - B$; $B - V$; the bolometric correction normalized to 0.0 for 7000, 1; the mean magnitudes in the *u*, *v*, *b*, and *y* passbands; $u - b$; $b - y$; m_1 ; c_1 . Table 5A lists the Matthews and Sandage *UBV*; Table 5B, the preferred Buser and Kurucz *UBV*.

TABLE 6.—Nine models are listed on each page, but four pages are required in order to list the 342 wavelengths for each model. The heading for each column gives the effective temperature, the log surface gravity, and the log metal abundance relative to solar. The first column lists the wavelength in nm. Each model column lists $\log F_{\lambda}$ ($\text{ergs cm}^{-2} \text{s}^{-1} \text{nm}^{-1}$) and the per mil blocking fraction $(1 - F_{\lambda}/F_{\lambda}^{\text{continuum}})$, which indicates the line absorption. Flux was not computed in the Lyman continuum for the coolest models, so the columns for those models are filled out with 0.0000. Below we list the factors by which to multiply our fluxes to convert to other units:

| | |
|-----------------------------|--|
| F_{λ} (nm $^{-1}$) | 1. |
| F_{λ} (Å $^{-1}$) | 0.1 |
| F_{λ} (μm $^{-1}$) | 1000. |
| F_{λ} (cm $^{-1}$) | 10 7 |
| Flux moment | H_{λ} (nm $^{-1}$ sr $^{-1}$) |
| Physical flux | \mathcal{F}_{λ} (nm $^{-1}$) |
| Flux at Earth | f_{λ} (nm $^{-1}$) |
| Photon flux at Earth | N_{λ} (nm $^{-1}$) |
| | F_{ν} (Hz $^{-1}$) |
| | F_{ν} [(cm $^{-1}$) $^{-1}$] |

where λ is in nm, R_* is the stellar radius, d is the stellar distance, and θ is the stellar angular diameter in milli-arcsec.

TABLE 8.—H α , H β , H γ , and H δ line profiles are listed for each model. The table for each line runs for six pages listing all the models. For each model are given the effective temperature, log surface gravity, log metal abundance relative to solar, equivalent width in nm, and 27 values of residual flux in per mil for the wavelength displacements from line center in nm that are listed at the top of each page. A residual flux labeled "000" stands for 1000. The profiles are normalized to 1000 at ± 10 nm from line center. If these profiles are to be compared to observed profiles that are operationally defined relative to some other displacement from line center, the profiles and equivalent widths must be renormalized.

(This Page Intentionally Left Blank)

TABLE 4
THE MODELS

| MASS | TAU ROSS | TAU 500 | TEFF | 5500* | LOG G | 0.00 | LOG ABUND | .00 | CONVECTIVE | | | P | ACC RAD | CONV FRAC |
|------|-------------|------------|---------|---------|--------|--------|-----------|---------|------------|---------|---------|--------|------------|--------------|
| | | | | | | | | | X | T | P | NE | NA | RHO |
| 1 | -38761 | 0.0000 | 0.0000 | 0.0000 | 3000.3 | -3893 | 7.7323 | 11.9934 | -11.6635 | -4.1046 | -3.3399 | .0865 | -2.6844 | -27.0123 |
| 2 | -22215 | -4.3268 | -3.5621 | 10.9100 | 3765.6 | -2238 | 8.0766 | 12.0603 | -11.5966 | -4.1046 | -3.3399 | .0866 | -2.8477 | -29.3451 |
| 3 | -06172 | -4.1624 | -3.4012 | 11.2337 | 3816.9 | -0632 | 8.2353 | 12.2150 | -11.4419 | -4.0797 | -3.3373 | .0868 | -2.8742 | 0.0000 |
| 4 | .09200 | -3.9979 | -3.2464 | 11.4124 | 3867.2 | .0906 | 8.3877 | 12.3631 | -11.2938 | -4.0517 | -3.3340 | .0869 | -2.8817 | 0.0000 |
| 5 | .24067 | -3.8327 | -3.0958 | 11.5345 | 3915.9 | .2393 | 8.5535 | 12.5064 | -11.1505 | -4.0203 | -3.3298 | .0872 | -2.8864 | 0.0000 |
| 6 | .38470 | -3.6673 | -2.9491 | 11.6280 | 3964.2 | .3835 | 8.6790 | 12.6452 | -11.0117 | -3.9846 | -3.3244 | .0875 | -2.8897 | 0.0000 |
| 7 | .52497 | -3.5007 | -2.8053 | 11.7038 | 4013.3 | .5239 | 8.8195 | 12.7803 | -10.8766 | -3.9435 | -3.3177 | .0879 | -2.8824 | 0.0000 |
| 8 | .65991 | -3.3347 | -2.6658 | 11.7668 | 4064.7 | .6588 | 8.9565 | 12.9096 | -10.7472 | -3.8969 | -3.3092 | .0885 | -2.8735 | 0.0000 |
| 9 | .78968 | -3.1691 | -2.5302 | 11.8205 | 4118.0 | .7887 | 9.0903 | 13.0339 | -10.6230 | -3.8447 | -3.2986 | .0892 | -2.8674 | 0.0000 |
| 10 | .91489 | -3.0032 | -2.3979 | 11.8672 | 4172.3 | .9139 | 9.2217 | 13.1534 | -10.5034 | -3.7875 | -3.2856 | .0902 | -2.8623 | 0.0000 |
| 11 | 1.03612 | -2.8363 | -2.2678 | 11.9086 | 4227.2 | 1.0350 | 9.3508 | 13.2689 | -10.3880 | -3.7254 | -3.2698 | .0915 | -2.8573 | 0.0000 |
| 12 | 1.15290 | -2.6693 | -2.1403 | 11.9455 | 4282.3 | 1.1520 | 9.4776 | 13.3802 | -10.2767 | -3.6586 | -3.2507 | .0932 | -2.8511 | 0.0000 |
| 13 | 1.26459 | -2.5035 | -2.0158 | 11.9785 | 4336.6 | 1.2636 | 9.6009 | 13.4864 | -10.1705 | -3.5887 | -3.2281 | .0952 | -2.8435 | 0.0000 |
| 14 | 1.37272 | -2.3372 | -1.8923 | 12.0086 | 4390.3 | 1.3720 | 9.7221 | 13.5894 | -10.0675 | -3.5151 | -3.2015 | .0979 | -2.8300 | 0.0000 |
| 15 | 1.47727 | -2.1706 | -1.7695 | 12.0361 | 4444.0 | 1.4765 | 9.8415 | 13.6887 | -9.9682 | -3.4382 | -3.1705 | .1012 | -2.8094 | 0.0000 |
| 16 | 1.57875 | -2.0033 | -1.6466 | 12.0616 | 4498.2 | 1.5781 | 9.9599 | 13.7849 | -9.8720 | -3.3578 | -3.1347 | .1056 | -2.7844 | 0.0000 |
| 17 | 1.67655 | -1.8368 | -1.5239 | 12.0851 | 4552.7 | 1.6759 | 10.0766 | 13.8775 | -9.7794 | -3.2751 | -3.0940 | .1111 | -2.7501 | 0.0000 |
| 18 | 1.77126 | -1.6731 | -1.4005 | 12.1069 | 4609.4 | 1.7706 | 10.1937 | 13.9668 | -9.6901 | -3.1886 | -3.0477 | .1183 | -2.7084 | 0.0000 |
| 19 | 1.86290 | -1.5033 | -1.2758 | 12.1273 | 4669.6 | 1.8622 | 10.3128 | 14.0528 | -9.6041 | -3.0981 | -2.9948 | .1277 | -2.6603 | 0.0000 |
| 20 | 1.95141 | -1.3361 | -1.1494 | 12.1463 | 4734.2 | 1.9507 | 10.4347 | 14.1353 | -9.5216 | -3.0030 | -2.9349 | .1400 | -2.6041 | 0.0000 |
| 21 | 2.03635 | -1.1690 | -1.0214 | 12.1641 | 4805.4 | 2.0354 | 10.5618 | 14.2136 | -9.4433 | -2.9014 | -2.8664 | .1560 | -2.5369 | 0.0000 |
| 22 | 2.11679 | -1.0025 | -.8921 | 12.1806 | 4887.2 | 2.1159 | 10.6983 | 14.2867 | -9.3702 | -2.7899 | -2.7866 | .1770 | -2.4535 | 0.0000 |
| 23 | 2.19226 | -.8352 | -.7606 | 12.1957 | 4985.6 | 2.1912 | 10.8505 | 14.3533 | -9.3036 | -2.6635 | -2.6908 | .2045 | -2.3524 | 0.0000 |
| 24 | 2.26091 | -.6684 | -.6278 | 12.2094 | 5104.6 | 2.2598 | 11.0228 | 14.4116 | -9.2452 | -2.5191 | -2.5752 | .2399 | -2.2302 | 0.0000 |
| 25 | 2.32138 | -.5017 | -.4937 | 12.2214 | 5252.7 | 2.3201 | 11.2225 | 14.4595 | -9.1974 | -2.4388 | -2.4330 | .2852 | -2.0776 | 0.0000 |
| 26 | 2.37239 | -.3348 | -.3581 | 12.2315 | 5346.9 | 2.3707 | 11.4538 | 14.4949 | -9.1620 | -2.1474 | -2.2590 | .3423 | -1.8891 | -15.8934 |
| 27 | 2.41322 | -.1676 | -.2211 | 12.2398 | 5665.4 | 2.4111 | 11.7184 | 14.5171 | -9.1397 | -1.9119 | -2.0496 | .4129 | -1.6641 | -11.7676 |
| 28 | 2.44392 | .0003 | -.0827 | 12.2462 | 5949.4 | 2.4411 | 12.0175 | 14.5252 | -9.1317 | -1.6340 | -1.7996 | .4984 | -1.3922 | -9.4069 |
| 29 | 2.46531 | .1680 | .0554 | 12.2509 | 6289.4 | 2.4613 | 12.3377 | 14.5198 | -9.1370 | -1.3151 | -1.5122 | .5997 | -1.0676 | -6.8868 |
| 30 | 2.47827 | .3501 | .2030 | 12.2539 | 6821.0 | 2.4723 | 12.7648 | 14.4903 | -9.1666 | -8.8392 | -1.0759 | .7300 | -5.5761 | -3.4201 |
| 31 | 2.48334 | .5179 | .3379 | 12.2553 | 7434.8 | 2.4749 | 13.1726 | 14.4408 | -9.2161 | -3.3059 | -3.5745 | .8519 | -1.1430 | -6.293 |
| 32 | 2.48630 | .6750 | .4683 | 12.2561 | 7747.5 | 2.4758 | 13.3487 | 14.4105 | -9.2464 | -3.0486 | -3.3268 | .9345 | -1.1604 | -2.2772 |
| 33 | 2.48925 | .8481 | .6186 | 12.2570 | 7977.0 | 2.4768 | 13.4636 | 14.3859 | -9.2710 | -1.284 | -1.533 | .9973 | -1.2276 | -1.388 |
| 34 | 2.49196 | 1.0076 | .7623 | 12.2579 | 8180.2 | 2.4781 | 13.5561 | 14.3623 | -9.2946 | 2.767 | -3.0074 | 1.0427 | -1.2679 | -1.0704 |
| 35 | 2.49494 | 1.1722 | .9149 | 12.2589 | 8358.4 | 2.4796 | 13.6297 | 14.3401 | -9.3168 | .3974 | .1129 | 1.0835 | -1.3202 | -1.0561 |
| 36 | 2.49825 | 1.3368 | 1.0713 | 12.2602 | 8542.8 | 2.4814 | 13.6983 | 14.3160 | -9.3409 | .5115 | 2.2285 | 1.1218 | -3.378 | -1.0309 |
| 37 | 2.50200 | 1.5023 | 1.2316 | 12.2616 | 8728.2 | 2.4836 | 13.7596 | 14.2905 | -9.3664 | .6156 | 3.3435 | 1.1604 | -3.3567 | -1.0259 |
| 38 | 2.50634 | 1.6686 | 1.3952 | 12.2635 | 8929.2 | 2.4861 | 13.8166 | 14.2623 | -9.3946 | .7142 | .4361 | 1.2003 | -3.3582 | -1.0215 |
| 39 | 2.51138 | 1.8343 | 1.5600 | 12.2657 | 9149.3 | 2.4891 | 13.8684 | 14.2312 | -9.4256 | .8029 | .5292 | 1.2400 | -3.3364 | -1.0116 |
| 40 | 2.51745 | 2.0009 | 1.7287 | 12.2687 | 9422.9 | 2.4923 | 13.9173 | 14.1936 | -9.4633 | .8822 | .6191 | 1.2963 | -2.8289 | -1.0222 |
| 41 | 2.43536 | 0.0000 | 0.0000 | 0.0000 | 3018.3 | .0641 | 8.0867 | 12.4443 | -11.2126 | -4.0434 | -3.3305 | .0869 | -2.5328 | -28.9436 |
| 42 | 2.27246 | -4.3158 | -3.6030 | 10.4062 | 3821.2 | .2271 | 8.5128 | 12.5048 | -11.1521 | -4.0434 | -3.3305 | .0870 | -2.7018 | -31.3171 |
| 43 | 3.11824 | -4.1558 | -3.4479 | 10.7252 | 3871.6 | .3813 | 8.6540 | 12.6533 | -11.0036 | -4.0058 | -3.3248 | .0872 | -2.7319 | 0.0000 |
| 44 | .02773 | -3.9940 | -3.2995 | 10.9007 | 3922.4 | .5272 | 8.8074 | 12.7936 | -10.8633 | -3.9642 | -3.3178 | .0874 | -2.7414 | 0.0000 |
| 45 | .16788 | -3.8298 | -3.1555 | 11.0206 | 3971.0 | .6675 | 8.9453 | 12.9285 | -10.7284 | -3.9183 | -3.3090 | .0876 | -2.7488 | 0.0000 |
| 46 | .30213 | -3.6649 | -3.0159 | 11.1118 | 4018.4 | .8017 | 9.0781 | 13.0576 | -10.5993 | -3.8677 | -3.2983 | .0880 | -2.7433 | 0.0000 |
| 47 | .43068 | -3.4999 | -2.8805 | 11.1850 | 4067.0 | .9303 | 9.2057 | 13.1810 | -10.4759 | -3.8130 | -3.2854 | .0884 | -2.7373 | 0.0000 |
| 48 | .55425 | -3.3347 | -2.7484 | 11.2461 | 4116.3 | 1.0538 | 9.3294 | 13.2992 | -10.3576 | -3.7545 | -3.2701 | .0890 | -2.7335 | 0.0000 |
| 49 | .67341 | -3.1692 | -2.6188 | 11.2984 | 4165.9 | 1.1732 | 9.4496 | 13.4134 | -10.2435 | -3.6921 | -3.2520 | .0897 | -2.7307 | 0.0000 |
| 50 | .78901 | -3.0028 | -2.4907 | 11.3442 | 4215.5 | 1.2887 | 9.5675 | 13.5238 | -10.1331 | -3.6260 | -3.2306 | .0907 | -2.7277 | 0.0000 |
| 51 | .90127 | -2.8356 | -2.3636 | 11.3850 | 4264.9 | 1.4009 | 9.6830 | 13.6309 | -10.0260 | -3.5567 | -3.2056 | .0919 | -2.7233 | 0.0000 |
| 52 | 1.00911 | -2.6698 | -2.2384 | 11.4212 | 4313.2 | 1.5088 | 9.7949 | 13.7339 | -9.9230 | -3.4856 | -3.1773 | .0934 | -2.7172 | 0.0000 |
| 53 | 1.11397 | -2.5038 | -2.1134 | 11.4542 | 4360.9 | 1.6136 | 9.9047 | 13.8340 | -9.8229 | -3.4121 | -3.1450 | .0953 | -2.7084 | 0.0000 |
| 54 | 1.21589 | -2.3379 | -1.9884 | 11.4843 | 4407.2 | 1.7156 | 10.0120 | 13.9313 | -9.7256 | -3.3365 | -3.1088 | .0977 | -2.6891 | 0.0000 |
| 55 | 1.31579 | -2.1710 | -1.8619 | 11.5121 | 4454.4 | 1.8155 | 10.1186 | 14.0266 | -9.6303 | -3.2583 | -3.0683 | .1008 | -2.6584 | 0.0000 |
| 56 | 1.41344 | -2.0036 | -1.7341 | 11.5380 | 4503.9 | 1.9132 | 10.2251 | 14.1195 | -9.5374 | -3.1775 | -3.0232 | .1049 | -2.6249 | 0.0000 |
| 57 | 1.50820 | -1.8371 | -1.6057 | 11.5620 | 4555.0 | 2.0077 | 10.3310 | 14.2092 | -9.4477 | -3.0950 | -2.9739 | .1102 | -2.5880 | 0.0000 |
| 58 | 1.60067 | -1.6705 | -1.4756 | 11.5845 | 4608.4 | 2.1004 | 10.4374 | 14.2967 | -9.3602 | -3.0103 | -2.9199 | .1171 | -2.5464 | 0.0000 |
| 59 | 1.69093 | -1.5039 | -1.3437 | 11.6055 | 4665.0 | 2.1906 | 10.5454 | 14.3816 | -9.2752 | -2.9230 | -2.8608 | .1262 | -2.4985 | 0.0000 |
| 60 | 1.77915 | -1.3367 | -1.2092 | 11.6255 | 4726.5 | 2.2788 | 10.6568 | 14.4641 | -9.1928 | -2.8318 | -2.7958 | .1382 | -2.4431 | 0.0000 |
| 61 | 1.86674 | -1.1693 | -1.0726 | 11.6442 | 4795.5 | 2.3644 | 10.7738 | 14.5434 | -9.1135 | -2.7349 | -2.7234 | .1540 | -2.3779 | 0.0000 |
| 62 | 2.194637 | -1.0030 | -.9351 | 11.6616 | 4875.7 | 2.4459 | 10.8999 | 14.6177 | -9.0391 | -2.6289 | -2.6414 | .1747 | -2.2971 | 0.0000 |
| 63 | 2.02360 | -.8360 | -.7957 | 11.6777 | 4973.8 | 2.5231 | 11.0430 | 14.6863 | -8.9706 | -2.5078 | -2.5442 | .2021 | -2.1983 | 0.0000 |
| 64 | 2.09439 | -.6689 | -.6552 | 11.6923 | 5096 | | | | | | | | | |